Research Square

Preprints are preliminary reports that have not undergone peer review.
They should not be considered conclusive, used to inform clinical practice,
or referenced by the media as validated information.

Spatial remodeling of the tumour microenvironment following neoadjuvant PD-1 blockade reveals an inducible tumour–immune engagement zone in head and neck cancer

N Gopalakrishna Iyer

gmsngi@nus.edu.sg

Cancer Therapeutics Research Lab, National Cancer Centre Singapore;Duke-NUS Medical School;Department of Head and Neck Surgery, Singapore General Hospital;Cancer Science Institute, NUS https://orcid.org/0000-0002-8812-6219

Lakshmi Alagappan

Cancer Therapeutics Research Lab, National Cancer Centre Singapore; Duke-NUS Medical School, Singapore https://orcid.org/0000-0003-0582-1513

Rachel Brooker

Liverpool Head & Neck Centre, University of Liverpool; Clatterbridge Cancer Centre NHS Foundation Trust

Hong Sheng Quah

Cancer Therapeutics Research Lab, National Cancer Centre Singapore; Duke-NUS Medical School, Singapore https://orcid.org/0000-0001-8430-8528

Frances Greaney

Liverpool Head & Neck Centre, University of Liverpool

Keith Hunter

Liverpool Head & Neck Centre, University of Liverpool; Liverpool University Hospitals NHS Foundation Trust

Christian Ottensmeier

University of Liverpool https://orcid.org/0000-0003-3619-1657

Max Robinson

The Newcastle upon Tyne Hospitals NHS Foundation Trust https://orcid.org/0000-0003-4491-6865

Fernando Kanishka

Cancer Therapeutics Research Lab, National Cancer Centre Singapore

Jingwen Yu

Cancer Therapeutics Research Lab, National Cancer Centre Singapore; Duke-NUS Medical School, Singapore

Eliza Li Shan Fong

Department of Biomedical Engineering, National University of Singapore

Neo Zhen Wei

Translational Research and Innovation Laboratory, Division of Pathology, Singapore General Hospital, Singapore

Craig Ryan Joseph

Integrated Central Operations and Research Enablers, Agency for Science, Technology and Research (A*STAR)

Li Yen Chong

Agency for Science Technology and Research (A*STAR) https://orcid.org/0000-0002-4623-4633

Poh Joe Yeong

Duke-NUS Medical School; Translational Research and Innovation Lab, Division of Pathology, Singapore General Hospital;Institute of Molecular and Cell Biology, A*STAR; Department of Microbiology, SGH

Thomas Peters

Liverpool Head & Neck Centre, University of Liverpool https://orcid.org/0009-0005-2472-9706

Jaya Thomas

University of Southampton

Ian Reddin

University of Southampton

Anoop Haridass

Clatterbridge Cancer Centre NHS Foundation Trust

Claire Paterson

Beatson West of Scotland Cancer Centre

James McCaul

Queen Elizabeth University Hospital Glasgow

Martin Forster

University College Hospital London & University College London

Charlotte Rawcliffe

Liverpool Clinical Trials Centre (LCTC)

Richard Jackson

Liverpool Clinical Trials Centre (LCTC)

Jessica Green

Liverpool Clinical Trials Centre (LCTC)

Julie Perry

Liverpool Clinical Trials Centre (LCTC)

Maria Maguire

Clatterbridge Cancer Centre NHS Foundation Trust

Cliburn Chan

Duke-NUS Medical School, Singapore; Department of Biostatistics and Bioinformatics, Duke University School of Medicine

Joseph J Sacco
Liverpool Head & Neck Centre, University of Liverpool; Clatterbridge Cancer Centre NHS Foundation Trust https://orcid.org/0000-0003-2591-9796
Andrew Schache
Liverpool Head & Neck Centre, University of Liverpool; Liverpool University Hospitals NHS Foundation Trust

---

Article

Keywords:

Posted Date: September 11th, 2026

DOI: https://doi.org/10.21203/rs.3.rs-10709977/v1

License: This work is licensed under a Creative Commons Attribution 4.0 International License.
Read Full License

Additional Declarations: Yes there is potential Competing Interest. NGI sits on the Scientific Advisory Boards of VerImmune and Vivo Surgical and has received honoraria/funding from Merck/MSD and Innokeys, all of which are outside the scope of this submitted work. AS has sat on Scientific Advisory Boards and Consultancy Panels for MSD, receiving associated honoraria. JJS has received honoraria (personal and institution) for participation in advisory boards from BMS, Immunocore, Replimune, Pierre Fabre and Delcath, has received support for travel/conference attendance from BMS, MSD and Replimune, and has received grant income (to institution) for clinical trials from BMS, AZ and Immunocore. MDF reports research grants from AstraZeneca (Inst), Boehringer Ingelheim (Inst) and MSD (Inst); non-exec board member for Curacell; holds appointments with DRA and HCA; and has received honoraria for advisory and consultancy work from Accord, Amgen, AstraZeneca, BeOne, Boxer, Celgene, GSK, Guardant Health, Immutep, Janssen, Merck, MSD, Oxford VacMedix, Regeneron, Roche, Societe Generale, Syncorp and Transgene; he is supported by the UCL/UCLH NIHR Biomedical Research Centre. FG is an employee of Miltenyi Biotec. The remaining authors declare no other competing interests.

Spatial remodeling of the tumour microenvironment following neoadjuvant PD-1 blockade reveals an inducible tumour–immune engagement zone in head and neck cancer

Lakshmi Alagappan*[1,2], Rachel Brooker*[3,4], Hong Sheng Quah[1,2], Frances Greaney[3], Keith Hunter[3,5], Christian Ottensmeier[3,4], Max Robinson[6], Fernando Kanishka[1], Jingwen Yu[1,2], Eliza Li Shan Fong[7], Neo Zhen Wei[8], Craig Ryan Joseph[9], Li Yen Chong[8], Poh Joe Yeong[2,8,10,11], Tom Peters[3], Jaya Thomas[12], Ian Reddin[12], Anoop Haridass[4], Claire Paterson[13], James McCaul[14], Martin Forster[15], Charlotte Rawcliffe[16], Richard Jackson[16], Jessica Green[16], Julie Perry[16], Maria Maguire[4], Cliburn Chan[2,17], Joseph J Sacco†[3,4], Andrew Schache†§[3,5] , N Gopalakrishna Iyer†§[1,2,18,19]

*Joint 1st Authors † Joint Senior Authors § Corresponding Authors

[1]Cancer Therapeutics Research Lab, National Cancer Centre Singapore
[2]Duke-NUS Medical School, Singapore
[3]Liverpool Head & Neck Centre, University of Liverpool
[4]Clatterbridge Cancer Centre NHS Foundation Trust
[5]Liverpool University Hospitals NHS Foundation Trust
[6]Newcastle Upon Tyne NHS Foundation Trust
[7]Department of Biomedical Engineering, National University of Singapore
[8]Translational Research and Innovation Laboratory, Division of Pathology, Singapore General Hospital, Singapore
[9]Integrated Central Operations and Research Enablers, Agency for Science, Technology and Research (A*STAR)
[10]Institute of Molecular and Cell Biology (IMCB), Agency for Science, Technology and Research (A*STAR), Republic of Singapore
[11]Department of Microbiology, Singapore General Hospital, Singapore
[12]University of Southampton
[13]Beatson West of Scotland Cancer Centre
[14]Queen Elizabeth University Hospital Glasgow
[15]University College Hospital London & University College London
[16]Liverpool Clinical Trials Centre (LCTC)
[17]Department of Biostatistics and Bioinformatics, Duke University School of Medicine
[18]Department of Head and Neck Surgery, Singapore General Hospital
[19]Cancer Science Institute, National University of Singapore

Correspondence should be addressed to N. Gopalakrishna Iyer (gmsngi@nus.edu.sg) and Andrew Schache (schache@liverpool.ac.uk)

Abstract

Perioperative PD1-blockade has become standard-of-care for locally-advanced head and neck squamous cell carcinoma(SCC), yet functional biomarkers remain undefined. Here we report outcomes from the NICO trial(NCT03721757;ISRCTN17428671), where oral SCCs were excised within 14 days of nivolumab treatment. Integrating pathologic, bulk and spatial data across matched pre- and on-treatment tumour tissue, we find that response is defined by spatial reorganisation of the $CD8^+$ compartment: depletion of dysfunctional states, accumulation of naïve and effector-memory cells, and emergence of an inducible tumour–immune engagement zone(iTIEZ). The iTIEZ extended three to eight cell diameters beyond the tumour-immune contact boundary, was enriched for cytotoxic and activation programmes, and adjacent to plasma-cell-rich niches, while fibroblast-rich niches were prominent in the Non-response group . These patterns were validated across a range of datasets, supporting the role of the iTIEZ as a spatial unit for immune-checkpoint blockade treatment-response, providing insights into potential combinatorial strategies and biomarker-driven treatment stratification.

Introduction

Perioperative immune checkpoint blockade (ICB) have reshaped the therapeutic landscape of solid tumours[1–4]. This is especially true in head and neck squamous cell carcinoma (HNSCC), a disease in which five year overall survival in locally advanced disease has remained below 50% for more than two decades[5]. Clinical development of ICB progressed stepwise from the recurrent/metastatic to the curative intent setting[6,7]. A series of phase Ib/II neoadjuvant trials demonstrated that one or two doses of anti-PD-1 therapy administered before definitive surgery did not compromise surgical timelines, elicited major pathological responses in a subset of patients, and pathological tumour regression was associated with reduced one-year relapse rates in high-risk, HPV-unrelated disease[8,9]. These culminated in the KEYNOTE-689 study, which established perioperative pembrolizumab as a new standard of care, demonstrating significantly improved event free survival, driven by a reduction in distant metastases[10]. This supports the hypothesis that immune priming in the presence of an intact primary tumour and draining lymph nodes enhances systemic anti-tumoural immunity.

Having established the role of neoadjuvant PD-1 blockade in the curative armamentarium, critical questions include the optimum duration of treatment, as well as how to determine which patients achieve sufficient pathological response to permit treatment deescalation whilst sustaining durable systemic benefit, compared to those that derive little or no benefit and may require combinatorial treatment or alternative treatment regimens. No existing biomarker, including PD-L1 staining or combined positive score (CPS), tumour mutational burden (TMB), or HPV status adequately stratifies patients to answer any of these questions[11]. Mechanistic or functional biomarkers based on spatial and cellular programmes that underlie effective immune priming could inform patient selection, guide rational combination therapies, and support future treatment de-escalation strategies.

The basis for neoadjuvant immune modulation rests on reinvigorating immune effectors within the primary tumour microenvironment in the presence of the tumoural antigen repertoire and with intact immune structures, promoting a more directed antitumour response. Proposed mechanisms include reactivation of memory T cell populations and primary priming of naïve cytotoxic T cells against tumour antigens released during early tumour cell death[12,13]. Demonstrating these mechanisms directly

has been critically constrained for two principal reasons. First, most translational studies have relied on bulk transcriptomic profiling or dissociated single cell sequencing alone, neither of which preserves the spatial relationships between tumour infiltrating lymphocytes (TILs) and malignant epithelium, tertiary lymphoid structures, and other key tissue microenvironments[14]. Spatially resolved transcriptomic technologies permit simultaneous interrogation of thousands of transcripts while preserving tissue architecture, enabling reconstruction of cellular neighbourhoods, ligand–receptor interactions, and niche-specific transcriptional programmes[15,16]. Second, the majority of translational studies have profiled surgical specimens obtained several weeks after treatment with neoadjuvant ICB. Although these samples effectively capture persistent tumour and immune evasion mechanisms in nonresponders, they are obtained after substantial tumour and immune cell regression has already occurred in responding patients. Preclinical orthotopic models have shown that the dominant effects of neoadjuvant PD-1 blockade are established within the first one to two weeks of treatment[17–19], suggesting that very early tissue sampling is essential to capture immune initiation rather than downstream consequences of tumour regression. Therefore, in order to identify mechanistic biomarkers, profiling should focus on matched pre-treatment and, very early, on treatment tissue to be collected during the narrow window in which immune remodelling is actively occurring, before tumour regression and subsequent tissue reorganisation obscure the mechanisms responsible for therapeutic success[20,21].

Here we report the results of the prospective multicentre phase II Neoadjuvant and adjuvant nivolumab as Immune Checkpoint inhibition in Oral cavity cancer (NICO) trial[22] and leverage the unique bioresource to define the earliest spatial determinants of response to neoadjuvant PD-1 blockade in resectable oral squamous cell carcinoma (OSCC). The trial incorporated matched pretreatment biopsies and surgical resection specimens, collected within two weeks of the administration of a single dose of nivolumab (NIVO), providing a rare opportunity to examine immune remodelling during its earliest stages. By integrating paired spatial transcriptomics, spatial proteomics and complementary validation across independent tissue compartments, external datasets and patient derived explants, we define the cellular ecosystems and spatially restricted transcriptional programmes associated with early immune activation following PD-1 blockade.

Results

Clinical outcomes and translational resource generated by the NICO trial

Patients included in the translational analyses were recruited through the prospective multicentre phase II NICO trial (NCT03721757; ISRCTN17428671), which investigated perioperative single-agent nivolumab, in patients with resectable stage III or IV oral squamous cell carcinoma (**Fig. 1A-C**). Between May 2019 and November 2020, 23 patients were enrolled across two UK centres. The trial was discontinued early due to the impact of COVID on recruitment and funder decision to withdraw funding. The median age at enrolment was 62 years (range 23–73 years), 61% of participants were male, and all patients had locally advanced disease. Primary tumour sites included the mandible (39%), tongue (30%), floor of mouth (17%), and other oral cavity subsites. Baseline demographic and clinicopathological characteristics of the study cohort are summarized in **Supp Table S1**.

Twenty-two participants received nivolumab and twenty subsequently underwent radical surgical resection (**Fig. 1D**). The trial protocol uniquely incorporated paired tissue acquisition, comprising diagnostic biopsies obtained before treatment together with matched surgical specimens collected no more than 14 days after a single dose of nivolumab. The formal primary endpoint analysis yielded a 12 month disease-free survival (DFS) rate of 84.0% (95% CI 59.0-95.0). An updated post-hoc analysis accounting for subsequent follow-up and resolved censoring demonstrated DFS rates of 85.0% (95% CI 60.4–94.9) at 12 months and 80.0% (95% CI: 55.1–92.0) at 24 months. These figures numerically exceed historical outcomes in this patient group but our data is limited by the small sample size[10]. Following the ethically-approved extended follow-up analysis (Ethics committee references; 10/H1002/53 & 23/NW/0348), only two disease recurrences were observed during protocol defined follow up, with a single additional recurrence identified after 24 months; DFS 80.0% (95% CI 55.1-92.0) (**Fig. 1E**). Treatment related adverse events and surgical complications were comparable to those described in other, larger, studies and are reported along with protocol compliance in **Supp Table S2-S3**.

Targeted bulk RNA-seq identifies a ΔTIL-aligned transcriptional axis defining response states

23 patients were enrolled on the trial, of whom 22 were treated with nivolumab and 20 underwent surgery and paired tissue collection. 19 patients with available paired pre-treatment and surgical FFPE tissue of sufficient quality were included in the downstream spatial transcriptomic analyses (Ethics committee references; 21/SC/0148). Bulk RNA sequencing and COMET spatial proteomic analyses were performed on matched samples from 18 patients while whole genome sequencing was performed on 12 patients reflecting tissue availability and quality for each assay. A schematic overview of the cohort design, treatment timeline, tumour types, and multi-omics profiling strategy is shown in **Supp Fig. 2A.**

Bulk DNA whole-genome sequencing (WGS) was performed on surgical primary tumours (n=12), and showed the expected mutational profile dominated by TP53 mutations in 66.7% of patients with a median tumour mutational burden of 3.05 mutations/Mb (range, 0.3 – 7.9 mutations/Mb) (**Supp Table S4**).

Targeted bulk RNA-seq was performed on pre- and post-NIVO primary tumour specimens (n=42). Principal component analysis (PC1–PC4) of patient-specific log2 fold-change profiles revealed variation in transcriptional response profiles across patients (**Supp Fig. 2B).** Among these components, PC3 captured a major axis of variation that independently aligned with pathologic ΔTIL status data and limited pathologic response data (**Supp Fig. 2B, Fig. 2A**). The PC3-associated gradient of treatment-related transcriptional variation was driven by genes associated with immune activation and interferon-response (e.g., *ISG15, IFIT1, CXCL13, CD3E, HLA-DRA*) on one hand (associated with lower arbitrary PC3 value), alongside epithelial and stromal programs (e.g., *KRT5, KRT16, COL1A1, ITGA6*), which associated with higher PC3 and less favourable immune signalling patterns **(Fig. 2B)**.

Using PC3 as a classifier, we observed patients with a low PC3 value clustered with positive ΔTIL anchor cases (including the 2 pathologic exceptional responders), which we classified as patients with an immune response (Response group), whereas those clustering with negative ΔTIL anchor cases were classified as patients with an immune non-response (Non-response group) (**Fig. 2C**). This classification was used for all downstream comparative analyses. Of the 19 patients included in the spatial analyses, 12 were deemed to be in the Response group, which is consistent with response proportion data seen in previous neo-adjuvant studies[8,9].

Single cell spatial proteomic atlas of the tumour microenvironment

Tissue microarrays (TMA) were constructed using paired specimens from 19 patients, comprising four tumour tissue compartments (hereafter referred to as tumour types for simplicity) analysed throughout this study: primary tumour before nivolumab (pre-NIVO primary), primary tumour after nivolumab (post-NIVO primary), 'pathologically defined' advancing front after nivolumab (post-NIVO adv front) and normal tissue after nivolumab (post-NIVO normal) as described in the **Methods** below. Single cell spatial transcriptomic profiling was performed using the CosMX 6K platform to generate a high resolution cellular map of the tumour microenvironment. Initial quality control assessed total counts, detected genes, and control probe distributions across samples. Following filtering, normalization, and batch correction, technical variation was reduced while preserving biological structure, resulting in a harmonized single cell expression dataset for downstream analysis (**Supp Fig. 2C–2D**).

Dimensionality reduction was performed using principal component analysis (PCA), followed by Uniform Manifold Approximation and Projection (UMAP)[23]. UMAP embedding revealed a well-structured transcriptional landscape. The embedding showed consistent global organization of cells following batch correction, and visualisation by patient and tumour type confirmed effective integration across samples without disrupting overall structure (**Supp Fig. 2E–2F**). The distribution of cells across tumour types was consistent across patients, further supporting robustness of integration (**Supp Fig. 2G**).

Unsupervised clustering of single cell transcriptomic profiles identified major cellular compartments spanning immune, tumour, and stromal populations as defined by canonical markers (**Fig. 2D**). These included B cells (*CD22, MS4A1, IGHM*), T cells (*CD3D, CD3E, CD3G, CD247*), plasma cells (*IGKC, IGHG1/2, IGLL5*), macrophages (*C1QA/B/C, CD74*), dendritic cells (*CD74, HLA-DRA, FCN1*), neutrophils (*CSF3R, CXCL8, G0S2*), mast cells (*CPA3, TPSAB1/2, HDC*), endothelial cells (*PECAM1, VWF*), fibroblasts (*COL1A1, COL3A1, COL1A2, COL6A1/2*), epithelial/tumour cells (*KRT14, KRT5, KRT17, KRT6A*), myogenic cells (*TTN, DES, CRYAB*), and neuronal cells (*CNTN5, CBLN2, CRHR2*), defining a comprehensive tumour microenvironment atlas. The distribution of these annotated cell types across patients demonstrated varying representation of all major compartments across the cohort (**Fig. 2E**). Dot plot analysis confirmed specific and consistent expression of lineage defining markers across annotated populations, supporting robust separation of major cell types (**Fig.**

2F). UMAP feature plots of canonical markers further validated compartment-specific expression patterns across the transcriptional landscape, confirming clear distinction of major immune, tumour, stromal, and tissue resident cell populations (**Supp Fig. 2H**). Together, these analyses define a well resolved single cell transcriptomic atlas of the tumour microenvironment, forming the basis for subsequent spatial and interaction-based analyses.

Treatment associated remodelling of tumour and immune cell composition across response groups

Treatment associated changes in cellular composition were next assessed across pre-NIVO and post-NIVO primary tumour samples, classified by Response and Non-response groups defined above. Changes in cell type proportions across conditions were visualized using alluvial plots (**Fig. 2G**), highlighting remodelling of the tumour microenvironment following the therapy. In the Response group, pre-NIVO to post-NIVO transitions were characterised by a reduction of tumour cells accompanied by expansion of plasma cells, with little to no change in the overall T cell compartment. In contrast, the Non-response group exhibited an opposing pattern: relative expansion of tumour cells and depletion of plasma cells following treatment. These opposing treatment associated changes should be interpreted in the context of baseline differences in cellular composition between the Response group and Non-response group, indicating that the two groups occupy distinct tumour microenvironment states *a priori*. These trends were quantified at the patient level by comparing the percentage of major cell types across matched pre-NIVO and post-NIVO samples (**Fig. 2H).** Consistent with the global pattern and supporting the classification algorithm, patients in the Response group showed a significant decrease in tumour cell abundance and a corresponding increase in plasma cell abundance following treatment, whereas patients in the Non-response group exhibited changes in the opposite direction.

Together, these analyses demonstrate that treatment response is associated with coordinated and opposing shifts in tumour and immune compartments, highlighting distinct trajectories of microenvironmental reorganisation in the Response and Non-response group.

Treatment-associated remodelling of CD8$^+$ T cell subtypes reveals distinct response archetypes

Following broad cell type annotation, we focused on T cells for downstream analysis, as they represent the primary effector compartment targeted by PD-1 blockade. Ambiguous T cells lacking detectable *CD4*, *CD8A* or *CD8B* expression were computationally resolved into CD4$^+$ and CD8$^+$ lineages using a supervised classification framework prior to subtype analysis (**Supplementary Fig. 3A - D; Methods**). CD8$^+$ T cells resolved into eight transcriptionally distinct subtypes, including tissue resident (CD8_T_TR), stem-like (CD8_T_SL), quiescent (CD8_T_Q), naïve (CD8_T_N), effector memory (CD8_T_EM), dysfunctional (CD8_T_DYS_1 and CD8_T_DYS_2), and cytotoxic dysfunctional (CD8_T_CYT_DYS) (**Fig. 3A**). These subtypes reflect a continuum from naïve and memory-associated programs (e.g. *LEF1, BTG1/2, IL7R, CCR7, SELL*) to cytotoxic and dysfunctional programs characterized by effector and exhaustion-associated gene expression (e.g. *GZMA, GNLY, ENTPD1, LGALS1, LGALS3*).

CD8$^+$ T cell subtypes were present across patients, with variable relative abundance, indicating heterogeneous composition of the CD8$^+$ compartment within the cohort (**Fig. 3B**). CD8$^+$ T cell annotation was supported by canonical marker expression patterns, confirming robust transcriptional identities across clusters (**Fig. 3C**). The same UMAP embedding further revealed multiple distinct subclusters within major CD8$^+$ T cell states, each characterised by discrete marker expression profiles (**Supp Fig. 3E**).

To assess treatment associated remodelling, changes in CD8$^+$ T cell subtype composition were evaluated between pre-NIVO and post-NIVO samples within the Response and Non-response groups (**Fig. 3D**). In the Response group, treatment was associated with a reduction of CD8_T_DYS_2, accompanied by increases in CD8_T_EM and CD8_T_N populations. The Non-response group exhibited contrasting expansion of CD8_T_DYS_2 with concomitant reductions in CD8_T_EM and CD8_T_N populations post-treatment. These opposing shifts were consistently reflected at the patient level, where paired comparisons across samples confirmed treatment associated changes in CD8$^+$ T cell subtype proportions within key functional compartments (**Fig. 3E**).

$CD8^+$ T cell subtype dynamics were further quantified at the patient level using Δ (Post–Pre) subtype proportions, summarizing treatment associated changes across paired samples (**Fig. 3F**). In the Response group, CD8_T_DYS_2 decreased consistently across all patients, accompanied by heterogeneous increases in CD8_T_EM, CD8_T_CYT_DYS, CD8_T_SL, and CD8_T_N. In contrast, patients in the Non-response group exhibited a more uniform pattern, characterised by expansion of CD8_T_DYS_2 and concomitant reductions in CD8_T_EM, CD8_T_SL, and CD8_T_N, indicating a lack of coordinated $CD8^+$ T cell remodelling following treatment.

The dynamics within individual patient tumours resolved into four recurring archetypes (**Fig. 3G**), comprising three Response-associated archetypes; all characterised by a reduction of CD8_T_DYS_2, and one Non-response associated archetype characterised by expansion of CD8_T_DYS_2 together with reduced CD8_T_N, CD8_T_SL and CD8_T_EM compartments. The Response associated archetypes included a replacement dominant pattern characterised by expansion of naïve (CD8_T_N) and stem-like (CD8_T_SL) with reduction in memory (CD8_T_EM) T cells; a revival-like pattern, marked by selective expansion of CD8_T_EM cells; and a mixed pattern, characterized by heterogeneous expansion of CD8_T_N, CD8_T_SL and CD8_T_EM compartments. Together, these archetypes provide a conceptual framework for $CD8^+$ T cell remodelling across treatment response states.

$CD4^+$ T cell subtype analysis identifies response-associated divergence in Th17 populations

$CD4^+$ T cells resolved into ten transcriptionally distinct subtypes (**Fig. 3H**), including central memory (CD4_T_CM), naïve (CD4_T_N), effector memory (CD4_T_EM), stem-like (CD4_T_SL), regulatory (CD4_T_REG), tissue resident (CD4_T_TR), follicular helper (CD4_T_TFH), CD4_T_Th17, CD4_T_Th9, and dysfunctional (CD4_T_DYS) populations. Additional subpopulations within major $CD4^+$ T cell states were observed, revealing multiple subclusters characterised by discrete marker expression profiles (**Supp Fig. 3F**). $CD4^+$ T cell subtypes were detected across patients, with variable relative abundances across the cohort (**Fig. 3I**).

To assess treatment associated dynamics, $CD4^+$ T cell state transitions were compared across pre-NIVO and post-NIVO samples within Response and Non-

response groups (**Supp Fig. 3G**). Most $CD4^+$ subtypes showed modest shifts; however, CD4_T_Th17 exhibited a distinct pattern, decreasing following treatment in the Response group but increasing in the Non-response group. This pattern was further confirmed at the patient level, where CD4_T_Th17 abundance decreased post treatment in the Response group but increased in Non-response group (**Fig. 3J**), indicating a response associated divergence in Th17 dynamics. These findings identify CD4_T_Th17 cells as the principal $CD4^+$ T-cell population exhibiting differential remodelling between response groups following neoadjuvant PD-1 blockade.

Spatial distribution and baseline organization of $CD8^+$ T cells relative to tumour proximity

$CD8^+$ T cell abundance exhibited a clear spatial gradient relative to tumour regions, with a progressive decrease in cell density with increasing distance from tumour cells with most (>75%) T cells within ~35 μm of the tumour (**Fig. 4A**). This trend was observed across the cohort, indicating a conserved spatial organization in which $CD8^+$ T cells preferentially accumulate in close proximity to tumour. In contrast, $CD4^+$ T cells displayed a more attenuated spatial gradient and a broader distribution across distance to tumour (**Supp Fig. 4A**), suggesting CD8+ T cells, specifically, are more selectively enriched at the tumour-immune interface.

To further resolve spatial composition within the $CD8^+$ compartment, subtype proportions were quantified across discrete tumour–distance bins (B0 to B4: B0 representing tumour neighbouring cells and B4 representing the most distant cells) and compared between pre-NIVO and post-NIVO conditions within Response and Non-response groups (**Fig. 4B**). In the Response group, treatment was associated with a relative increase in CD8_T_N and CD8_T_EM subtypes across spatial bins accompanied by a reduction in CD8_T_DYS_1. In contrast, the Non-response group exhibited the opposite trend, with a relative increase in CD8_T_DYS_1 and relative decrease in CD8_T_N and CD8_T_EM subtypes following treatment. These spatial composition shifts were supported by near versus far analyses at the field of view level, which showed concordant directional trends across key $CD8^+$ T cell subtypes in both Response and Non-response groups (**Supp Fig. 4B**). Together, these analyses define the baseline spatial distribution of $CD8^+$ T cell states across tumour-distance bins and

demonstrate that treatment-associated changes in in subtype composition and localisation differ according to response.

Treatment-associated spatial reorganization of CD8⁺ T cell subtypes

To quantify treatment associated spatial remodelling of CD8⁺ T cell subtypes, subtype specific spatial enrichment scores were calculated across distance to tumour cells (as a pseudo-continuous variable using smaller bin sizes) comparing post-NIVO and pre-NIVO subtype proportions within each spatial compartment (**Fig. 4C–D**). Distinct patterns of spatial reorganization emerged between Response and Non-response groups.

In the Response group, treatment was associated with broad enrichment of CD8_T_N, CD8_T_EM, and CD8_T_CYT_DYS states across the tumour–distance gradient, accompanied by depletion of dysfunctional populations, particularly CD8_T_DYS_2 (**Fig. 4C**). Specifically, there was widespread decrease in the latter compartment, while the enrichment of CD8_T_N and CD8_T_EM was prominent even beyond the tumour-immune interface. In contrast, the Non-response group exhibited persistent and increased enrichment of CD8_T_DYS_1 and CD8_T_DYS_2 in close proximity to regions of tumour, with reduced localisation of naïve and effector memory subtypes both at the tumour immune interface and the space distal to this, following treatment (**Fig. 4D**).

These findings indicate that the Response group exhibits coordinated spatial reorganization of the CD8⁺ T cell subtypes following treatment, characterised by enrichment of naïve, effector memory, and cytotoxic populations close to tumour cells, together with a broad reduction in dysfunctional states across the tumour landscape. Conversely, while changes in spatial organisation also occur in the Non-response group, these appear uncoordinated, and lead to persistence, and even increase, of tumour proximal dysfunctional CD8⁺ T cell states without a shift towards T cell with effector capabilities suggesting an early deficit in ICB induced T cell reprogramming.

Coordinated transcriptional program emerges at the induced tumour immune engagement zone (TIEZ) following treatment in the Response group

Spatial gene expression gradients were next examined across tumour distance bins to characterize transcriptional programs associated with tumour proximity. To provide

spatial context, tumour- and microenvironment-associated genes (with specific representation), including *KRT5* (epithelial), *IGKC* (B cells), *COL1A1* (fibroblasts), *PECAM1* (endothelial cells), and *CD68* (macrophages), were used to delineate transitions between tumour rich and surrounding tissue regions.

To characterise spatially organised immune states surrounding tumour cells, we operationally defined a tumour-immune engagement zone (TIEZ) as the peritumoural region located approximately 24–60 µm (200 – 500 CosMx pixel coordinates) from the nearest tumour cell centroid, representing a continuous spatial zone, rather than just a discrete tumour-immune interface boundary, over which tumour-immune interactions are organised. Using the median centroid to centroid distance between the cells across the dataset (~8 µm or ~67px) as a proxy for single cell spacing, this corresponds to an estimated 3–8 cell diameter from the tumour, capturing a multi-cellular peritumoural zone beyond immediate cell to cell contact.

In the Response group, $CD8^+$ T cell transcriptional programs emerged at the tumour-immune interface and extended into the TIEZ, which was characterized by the coordinated enrichment of cytotoxic (*GNLY, PRF1, GZMH, CCL5*), activation and checkpoint-associated genes (*LAG3, TIGIT, CTLA4, TOX*), and immune-interaction markers such as *CXCL13*. In contrast, the Non-response group exhibited substantially weaker spatial organization of these transcriptional programs at the tumour-immune interface, with reduced enrichment of cytotoxic, activation, and checkpoint associated genes and limited to no extension into the TIEZ (**Fig. 4E**).

Notably, these spatial patterns were only apparent after ICB treatment and were largely absent in pre-treatment samples from both groups (**Supp Fig. 4C**), indicating that coordinated immune engagement within the TIEZ emerged specifically following nivolumab treatment. We therefore refer to this treatment-induced transcriptionally active state within the TIEZ as the induced tumour immune engagement zone (iTIEZ), a feature predominantly observed in the Response group.

Distinct spatial niches characterise responder and non-responder $CD8^+$ T cells

To characterise the local neighbourhoods surrounding $CD8^+$ T cells, a representative spatial reconstruction from a sample in the Response group was first examined, illustrating the heterogeneous organisation of $CD8^+$ T cell states within the tumour microenvironment and highlighting close spatial association of naïve $CD8^+$ T cells with

plasma cell rich regions (**Fig. 4F**). This observation motivated a distance based spatial neighbourhood analysis to systematically define recurrent niche states based on the composition of neighbouring cells surrounding $CD8^+$ T cells (**Fig. 4G**). Unsupervised clustering of neighbourhood profiles identified five major spatial niches associated with CD8 T cells, corresponding to tumour rich, T cell rich, plasma cell rich, fibroblast rich, and neuronal rich.

Spatial niche composition varied across tumour cell distance bins and differed between response groups following treatment (**Fig. 4H**). Pretreatment comparisons showed no significant differences in niche distribution between response groups across spatial bins (**Supp Fig. 4D**), indicating that observed differences emerged following treatment.

As expected, $CD8^+$ T cells located within the tumour-neighbouring spatial bin (B0) were predominantly associated with tumour rich niches, reflecting their direct proximity to tumour regions. Beyond the immediate tumour boundary, $CD8^+$ T cell neighbourhood composition diverged between response groups. In the Response group, $CD8^+$ T cells were highly found in plasma rich niches, whereas in the Non-response group they were more frequently found in the fibroblast rich niches, particularly across intermediate tumour distance bins.

These observations were further supported by per (TMA) core quantification, which demonstrated significantly increased percentage of $CD8^+$ T cells located within plasma cell rich niches in the Response group and increased percentage of $CD8^+$ T cells located within fibroblast rich niches in the Non-response group within the B2 spatial bin (**Fig. 4I**), with similar trends observed across adjacent spatial bins (**Supp Fig. 4E**). Consistent patterns were also identified using cell-cell contact based niche analysis, indicating that these response associated microenvironmental differences were preserved even when considering only direct cell to cell interactions (**Supp Fig. 4F–4G**). Representative spatial reconstructions of a sample in the Non-response group further illustrated $CD8^+$ T cells embedded within fibroblast rich microenvironments, consistent with the niche based observations (**Supp Fig. 4H**).

Interestingly, $CD8^+$ T cells residing within plasma cell rich niches in the Response group were located at a distance of approximately 64 μm (or 4 cell diameter) from the

tumour, placing these cells immediately beyond the iTIEZ. To further characterize the composition of these plasma rich neighbourhoods, we compared the local cellular microenvironment surrounding $CD8^+$ T cells in direct contact with plasma cells to that of all other $CD8^+$ T cells. As expected, plasma cells were the most enriched neighbouring population. The microenvironment were additionally enriched for CD8_T_N, B cells, other $CD8^+$ and $CD4^+$ T cell populations, and endothelial cells, while tumour cells were markedly depleted, suggesting that direct plasma cell–$CD8^+$ T cell contacts occur within broader, organized immune neighbourhoods rather than isolated plasma cell aggregates (**Supp Fig. 4I**). The marked enrichment of naïve $CD8^+$ T cells within these neighbourhoods further suggests that plasma cell rich niches (likely representing tertiary lymphoid structures) may function as local "nurseries" for $CD8^+$ T cell priming and activation.

Distinct fibroblast associated ligand–receptor programs underlie response associated spatial communication

Spatially constrained ligand–receptor interactions were next evaluated across tumour, fibroblast, and $CD8^+$ T cell compartments within defined spatial distance bins, enabling comparison of communication programmes between the patients in the Response group and Non-response group (**Supp Fig. 4J**). Differential interaction analysis (ΔLR = NR − R) revealed distinct response-associated signalling axes across tumour–stromal–immune interfaces.

Patients in the Non-response group were characterised by enrichment of fibroblast associated interactions involving extracellular matrix and adhesion related signalling, including *COL1A1–SDC1*, *COL1A2–SDC1*, *COL4A1–CD44*, and *COL4A1–SDC1*, together with matrix-stabilising and chemokine associated interactions such as *LUM–ITGB1*, *PLAU–LRP1*, *MIF–CD74*, and *MIF–CXCR4*. These interactions were predominantly enriched across fibroblast–T cell and fibroblast–tumour compartments, consistent with a more structured stromal communication network. In contrast, patients in the Response group exhibited relative enrichment of ligand receptor interactions associated with matrix remodelling and dynamic adhesion states, including *VIM–CD44*, *MMP1–CD44*, *TIMP2–CD44*, and *LAMA4–CD44*, along with *COL6A2–ITGA3*. These signals were observed across fibroblast–T cell compartments spanning multiple spatial distance bins.

Together, these findings indicate that response associated differences in $CD8^+$ T cell spatial organisation are accompanied by distinct fibroblast driven communication programmes, with patients in the Non-response group enriched for stable extracellular matrix and immunomodulatory signalling, and patients in the Response group exhibiting a shift toward matrix remodelling associated interaction states.

Advancing front tissues recapitulate response associated spatial immune organization

To determine whether the spatial programs identified within primary central tumour regions were preserved within anatomically defined tumour edge, $CD8^+$ T cell spatial organization was evaluated in post-NIVO advancing front tissues, which were pathologically defined during TMA construction. Spatial gene expression gradients revealed a conserved tumour immune interface and iTIEZ characterised by enrichment of immune associated genes including *CCL5*, *TIGIT*, *CXCL13,* and *GNLY* in the Response group, whereas the Non-response group exhibited stronger *CXCL8* expression concentrated within tumour associated regions marked by *KRT5* and reduced enrichment of immune activation programs (**Fig. 5A**).

Consistent with observations in primary tumour samples, spatial niche analysis demonstrated distinct microenvironmental contexts surrounding $CD8^+$ T cells in the advancing front (**Fig. 5B**). $CD8^+$ T cells in the Response group were preferentially associated with plasma cell rich niches, whereas $CD8^+$ T cells in the Non-response group were more frequently located within fibroblast rich niches.

Spatial enrichment analysis similarly demonstrated enrichment of CD8_T_EM states and depletion of CD8_T_DYS_2 populations within tumour proximal regions in the Response group, whereas the Non-response group showed persistent enrichment of dysfunctional $CD8^+$ T cell states near the tumour-stromal interface (**Supp Fig. 5A–5B**). These observations were further supported by field of view level analyses, which confirmed significant tumour proximal enrichment of CD8_T_EM together with depletion of CD8_T_DYS_2 in the Response group (**Supp Fig. 5C**). Collectively, these findings demonstrate that the spatial and microenvironmental organization of $CD8^+$ T cells observed in the central primary tumour regions is preserved in the more peripheral advancing-front.

Spatial proteomics validates response-associated tumour immune interface programs

To validate transcriptomic observations using an orthogonal modality, matched tissue sections from the same patient cohort were profiled using COMET 40-plex spatial proteomics. Unsupervised clustering identified major cellular compartments corresponding to tumour, immune, and stromal populations, revealing cell type composition broadly consistent with the spatial transcriptomic dataset (**Fig. 5C–D**). Representative spatial reconstructions and canonical protein marker expression illustrated consistent cell type annotation across the dataset (**Supp Fig. 5D–E**).

Spatial protein expression gradients relative to tumour proximity revealed conserved tumour-immune interface and iTIEZ associated protein expression programmes that differed according to treatment response (**Fig. 5E and Supp Fig. 5F**). As expected, epithelial markers such as cytokeratin were enriched within tumour-associated regions. In the Response group, the TIEZ was characterised by enrichment of *CD8*, *LAG3*, *GZMB*, *Ki67*, *EOMES*, and *CD45RO*, consistent with activated, proliferative, cytotoxic and antigen-experienced T cell phenotypes localized near tumour regions. In contrast, the Non-response group exhibited relative enrichment of *PD1*, *ICOS*, and *FOXP3* closer to the tumour boundary, indicating a distinct immune context characterized by regulatory and dysfunctional immune states. Together, these findings provide orthogonal protein level validation of the tumour–immune interface and iTIEZ programmes identified by spatial transcriptomics.

External validation in cutaneous SCC confirms conserved spatial immune stromal organization

To evaluate whether spatial microenvironmental patterns were recapitulated within an independent cohort, a publicly available CosMx1k spatial transcriptomics dataset of cutaneous squamous cell carcinoma (with similar pre- and early on-ICB-treated samples) was analysed using the same analytical framework. Unsupervised clustering of the CosMx1k dataset identified major cellular compartments corresponding to tumour, immune, and stromal populations (**Fig. 5F**). Representative tissue reconstructions highlighted the relatively restricted spatial extent of sampling in this cohort, reflecting dense tumour foci and a compressed tumour–stromal architecture compared to our dataset (**Supp Fig. 5G**).

Spatial gene expression analysis using tumour distance profiling demonstrated structured spatial organisation of epithelial and immune associated markers. Cytokeratin (*KRT5*) was enriched within tumour proximal regions across samples. Immune activation markers including *LAG3*, *CXCL13*, *PRF1*, and *TOX* showed preferential localisation to the tumour immune interface and iTIEZ. Notably, in the Response group, these immune associated markers were more strongly concentrated within tumour proximal interface regions, whereas in the Non-response group, their expression appeared comparatively attenuated and shifted towards more distal compartments (**Fig. 5G**). Spatial niche analysis revealed differences in the distribution of microenvironmental contexts across response groups (**Fig. 5H–5I**). In particular, fibroblast rich niches were more frequent in the Non-response group, particularly within intermediate tumour distance compartments, whereas other niche states showed more heterogeneous distributions across samples.

These findings indicate that fibroblast associated spatial microenvironmental patterns observed in the primary NICO cohort are also reflected in an independent cSCC dataset, supporting the generalizability of spatial tumour stromal organisation across distinct squamous malignancies.

Ex vivo explant validation confirms spatial localization of TIEZ associated immune markers following PD-1 blockade

To functionally validate the spatial immune programmes identified in the NICO cohort, patient derived tumour explants were established from an independent cohort of six oral SCC patients. Explants were cultured ex vivo and treated with pembrolizumab for 5–7 days before immunofluorescence staining for PanCK, CD8 and candidate markers identified from the spatial transcriptomic analyses, including LAG3, CXCL8, CXCL13, PRF1, CCL5 and KLF2. Based on previously published response classifications, patients were assigned to Response group (P4–P6) or Non-Response group (P1–P3). Four of the six patients subsequently demonstrated concordant clinical responses to pembrolizumab treatment, providing independent clinical validation of the response group assignments[24].

Representative immunofluorescence images from the Response group demonstrated the formation of the iTIEZ characterized by CD8+ T cells positioned immediately adjacent to the tumour boundary (**Fig. 5J**). Within the iTIEZ, CD8+ T cells at or near

the tumour edge showed prominent expression of LAG3, CXCL8, CXCL13, PRF1, CCL5 and KLF2, recapitulating the spatial distribution observed in the primary NICO cohort. In contrast, explants from the Non-response group were largely dominated by PanCK-positive tumour regions, showed sparse CD8+ T-cell infiltration and lacked a clearly defined iTIEZ (**Supp Fig. SH**).

To quantitatively assess these spatial patterns, the normalised distance of each CD8+ T cell from the nearest tumour cell was calculated and marker expression was summarized across concentric spatial shells extending away from the tumour boundary (**Fig. 5K)**. Across explants from the response group, LAG3, CXCL8, CXCL13 and PRF1 consistently exhibited maximal expression within the iTIEZ rather than within the tumour core or distal stromal regions. Similar spatial distributions were observed for CCL5 and KLF2 (**Supp Fig. SI**), whereas explants from the Non-response group demonstrated reduced expression and a shift towards more distal tumour regions. Together, these findings provide *ex-vivo* validation that iTIEZ associated immune markers identified by spatial transcriptomics preferentially localise to the iTIEZ following PD-1 blockade, supporting this region as a functionally critical immune interface involved in therapeutic response.

Discussion

The NICO trial was designed and recruited before perioperative PD-1 blockade became standard of care in locally advanced HNSCC, and its protocol embedded a tissue collection window that would now be difficult to reproduce: a diagnostic biopsy taken before treatment and a surgical specimen taken within 14 days of a single dose of nivolumab. The trial was designed on the premise that even a brief period of PD-1 blockade would be sufficient to initiate tumour-specific immune priming while the primary tumour and draining lymph nodes remained intact. Although the trial has been superseded by KEYNOTE-689[10], its clinical signal is consistent with the latter, demonstrating exceptional pathological response in 2/22 patients who received neoadjuvant nivolumab (~10%), additional evidential immune response in 12/22 (~60%), 2-year DFS of 80 % whilst maintaining the timeline to definitive surgery without delay. The dataset is however unique, as almost all published translational analyses of neoadjuvant ICB tissue profile resection specimens obtained several weeks after treatment, by which point responding tumours have already regressed and the cellular machinery responsible has diminished and returned to baseline. Sampling at two weeks captures immune initiation rather than its aftermath.

Throughout these analyses, "Response" and "Non-response" denotes transcriptionally defined states, based on treatment associated expression changes aligned with ΔTIL-positive or ΔTIL-negative anchor, and limited (n=2) pathological response categories. With 23 patients enrolled (22 of whom received neoadjuvant nivolumab) and 3 recurrence events, the cohort is not powered to relate these states to disease free survival, and we did not observe such a relationship. The groups should therefore be read as descriptors of early immunological trajectory whose clinical significance remains to be established. With that caveat, the central observation of this study is that these two trajectories differ far more in the spatial organisation of the $CD8^+$ T cell compartment than in its size. The bulk classifier carries no positional information, and neither the tumour-distance organisation of $CD8^+$ states, the composition of $CD8^+$ cellular neighbourhoods, nor the protein level gradients measured by 40-plex imaging contributed to group assignment. That these mutually independent spatial measures separate the groups so consistently is the result we regard as robust.

Within the $CD8^+$ compartment, the most consistent treatment associated feature was depletion of the dysfunctional CD8_T_DYS_2 state, accompanied by variable expansion of naïve, stem-like, effector memory and cytotoxic dysfunctional populations that resolved into three recurring archetypes. The uniformity of the vacancy, set against the heterogeneity of what fills it, suggests that loss of the dysfunctional state is the shared event and its replacement is patient specific, arising through recruitment, local differentiation, or clonal replacement. In the absence of TCR sequencing we cannot distinguish between these possibilities, and the archetypes should be read as descriptive patterns rather than mechanisms, albeit patterns consistent with models of clonal replacement described in other settings of PD-1 blockade[25,26].

The organisation of this remodelling is what distinguishes the two trajectories most clearly. In the Response group, treatment was associated with a transcriptional programme arranged around the tumour boundary and extending approximately three to eight cell diameters into the surrounding tissue, the region we term the inducible tumour–immune engagement zone (iTIEZ). Within this zone, cytotoxic genes (*GNLY*, *PRF1*, *GZMH*, and *CCL5*) were co-enriched with activation- and checkpoint-associated genes (*LAG3*, *TIGIT*, *CTLA4*, *TOX*, and *CXCL13*). The equivalent organisation was weak or dysfunctional in the Non-response group, and critically, was largely absent from pretreatment tissue in both groups. The zone is therefore an induced organisational state rather than a pre-existing infiltrate that treatment merely reveals. In contrast, using scRNAse of dissociated tissue, Oliveira and colleagues[13] reported that pre-existing tumour resident T cells with cytotoxic potential associate with response to neoadjuvant anti-PD-1 in head and neck cancer, evidence for a pre-formed determinant of benefit as opposed to our data where we describe an induced state. However, these results are not necessarily contradictory. Our pretreatment specimens were not devoid of cytotoxic cells; what was absent was their coordinated positioning relative to the tumour boundary. A pre-existing reservoir of competent effectors may be necessary for the zone to form, while the zone itself is what blockade induces. Separating a permissive precondition from an induced organisation will require pre-treatment sampling at the spatial resolution applied here, ideally paired with TCR sequencing. Furthermore in their studies, post treatment specimens were obtained weeks after tumour regression and as such, non-informative in responders.

Three implications follow. First, response to PD-1 blockade is determined not simply by the presence of immune cells but by their arrangement relative to tumour tissue, a property rendered invisible to any assay that dissociates or averages across a specimen. Second, this offers a possible explanation for the inconsistent performance of individual biomarkers such as *CXCL13* and *LAG3* across studies; their significance may depend not on abundance but on where they are expressed relative to the tumour boundary, and on where in the tumour the tissue core was sampled. Third, the iTIEZ may constitute a more appropriate spatial unit for response assessment than conventional pathological constructs. The same zonal organisation was recapitulated in pathologically defined advancing front tissue, which suggests the advancing front is one location at which the zone can be observed, while the concept of an engagement zone is more pervasive than a histologic definition. This carries practical consequences for how tissue is selected for translational analysis.

Whether the iTIEZ forms at all appears to be conditioned by the surrounding stroma. Responding $CD8^+$ T cells preferentially occupied plasma-cell-rich neighbourhoods that were further enriched for B cells, additional T cell populations and endothelial cells, a composition consistent with tertiary lymphoid structures, and concordant with growing evidence linking such structures to immunotherapy benefit across tumour types[27–29]. Non-responding $CD8^+$ T cells were instead embedded within fibroblast rich niches, consistent with stromal contribution to a physiologic (rather than merely physical) immune exclusion[30,31]. These findings support the concept of stromal targeting strategies as rational combination partners for immune checkpoint blockade in excluded tumours.

Two features of these results bear directly on clinical translation. The zone was recoverable in advancing front tissue and in an independent cutaneous squamous cell carcinoma cohort treated with PD-1/PD-L1 blockade, suggesting it is neither an artefact of primary tumour core selection nor specific to oral cavity disease. And its constituent features were recovered at the protein level by 40-plex imaging and, in patient-derived explants, by a six marker immunofluorescence panel, meaning that assessing the zone does not mandate spatial transcriptomics. A panel comprising PanCK, CD8 and two or three of LAG3, CXCL13 and GZMB, read as a function of distance from the tumour boundary, is within the reach of a diagnostic laboratory.

Whether such a readout, measured on an on-treatment biopsy, identifies patients who may safely be deescalated or, indeed who require combination therapy is a testable question, and in our view the most useful next step.

Several limitations should be acknowledged. This was a small, single arm cohort from a trial, which closed early as a consequence of site activation delays and the unanticipated disruption caused by the COVID-19 pandemic, and all analyses are exploratory; comparisons were not corrected for multiple testing and should be interpreted as hypothesis generating. The absence of TCR sequencing precludes assessment of clonal replacement versus reinvigoration. Spatial thresholds, and the definitions of the tumour–immune interface and the iTIEZ, are operational constructs rather than biologically discrete boundaries. The external cSCC cohort differs in disease, therapeutic agent, gene panel and segmentation approach, and so supports the generalisability of these observations rather than confirming it. Finally, the early sampling window captures only the initiation of immune remodelling and speaks neither to its durability nor to the later effects of adjuvant nivolumab.

Collectively, these findings offer a biological framework for understanding early response to perioperative PD-1 blockade. Rather than a property of any individual immune population, the earliest correlate of response appears to be a reorganisation of the tumour–immune ecosystem: clearance of dysfunctional $CD8^+$ states, assembly of an activated tumour–immune interface, induction of an engagement zone extending several cell diameters into surrounding tissue, and the conditioning of all three by local stromal architecture. As perioperative immunotherapy enters routine practice, the clinical question shifts from whether to treat to whom to treat for how long and whether additional non anti-PD1 agents are needed.. A spatially defined, inducible readout measured early on treatment is a plausible foundation that may guide future patient stratification and rational combination therapies.

Methods

NICO trial

The Neoadjuvant and adjuvant nivolumab as Immune Checkpoint inhibition in Oral cavity cancer (NICO) trial[22] was a multicentre phase II non-randomised NICO trial

(NCT03721757; ISRCTN17428671), designed to investigate perioperative nivolumab (NIVO) in combination with standard of care surgery and risk-adapted adjuvant therapy for locally advanced oral cavity squamous cell carcinoma (OSCC).

The trial recruited patients from two UK centres: University Hospital Aintree/Clatterbridge Cancer Centre (Liverpool Head & Neck Centre) and Greater Glasgow & Clyde (The Beatson West Scotland Cancer Centre Glasgow). The study was sponsored by The Clatterbridge Cancer Centre NHS Foundation Trust and delivered in collaboration with the Liverpool Clinical Trials Centre. Ethical approval was obtained from the London - Harrow Research Ethics Committee (REC Ref. No. 18/LO/0368). Translational research studies associated with the NICO trial samples including investigation of molecular determinants of response and associated patient outcomes utilised additional ethical approvals (10/H1002/53, 21/SC/0148 and 23/NW/0328). Clinical Trial Authorisation was issued by the Medicines and Healthcare Products Regulatory Agency (MHRA). The clinical trial was funded by Bristol Myers Squibb (BMS). All patients provided signed informed consent to participate, which included permission to access tissue to undertake translational research protocols.

The trial was designed with two co-primary endpoints: 12-month disease-free survival (DFS), defined as disease recurrence or death within 12 months following surgery, and feasibility of recruitment. The original sample size calculation assumed that approximately one-third of enrolled patients would have high-risk pathological features, including extracapsular spread (ECS) or involved surgical margins, requiring adjuvant chemoradiotherapy (CRT). Based on a planned cohort of 120 patients, this corresponded to 40 high-risk patients. In this subgroup, the expected 12-month DFS following standard adjuvant therapy was estimated to be approximately 65%, and a DFS of ≥75% was considered clinically meaningful. Recruitment was terminated early (November 2020), in accordance with a trial funder's decision, following their acquisition of a separate corporate entity, which had a similar study that was closed and reporting. Consequently, the planned recruitment target was revised from 120 to 30 patients. With this reduced sample size, estimation of the 12-month DFS was expected to have substantially lower precision, with an approximate 95% confidence interval of ±20%.

Patients were enrolled according to predefined eligibility criteria. Patients were suitable for inclusion if diagnosed with operable T1-4 N1-3 or T3-4 N0 (AJCC 7th edition) biopsy

proven SCC oral cavity, WHO/ECOG (world health organisation/eastern cooperative oncology group) performance status score of 0-1 without contraindications to cisplatin chemotherapy. Exclusion criteria included suspected/apparent distant metastasis, previous active malignancy within the preceding 3 years, use of immunosuppressive agents, known HIV or Hepatitis (**Fig. 1B**).

Eligible patients received a single neoadjuvant dose of nivolumab (240 mg) 1–2 weeks prior to surgery, a further dose before adjuvant radiotherapy or chemoradiotherapy, followed by up to six adjuvant cycles of nivolumab (480mg) after completion of standard treatment (**Fig. 1C**).

Whole-genome sequencing

Genomic DNA was extracted from fresh-frozen tumour tissue and matched peripheral blood mononuclear cells (PBMCs) using the Maxwell® RSC Tissue DNA Kit (Promega) and Maxwell® RSC Buffy Coat DNA Kit (Promega), respectively. Whole-genome sequencing (WGS) was performed on tumour–normal pairs from 14 patients with head and neck squamous cell carcinoma. Following quality control, one patient was excluded because of a suspected tumour–germline sample mismatch. Although WGS data were available for one additional patient, these were not included in the present analyses because the primary tumour was deemed inoperable and, consequently, no matched CosMx spatial transcriptomic data were available. Sequencing reads were aligned to the GRCh38 human reference genome using BWA-MEM2 and processed using the nf-core/oncoanalyser pipeline. Somatic single-nucleotide variants and small insertions/deletions were identified using SAGE and functionally annotated using PAVE. Tumour mutational burden (TMB) was calculated as the total number of coding somatic mutations per tumour, and TMB and TP53 mutation status were extracted from the resulting somatic variant calls and incorporated as patient-level metadata for integration with the matched CosMx6k dataset.

Bulk RNA-seq processing and response classification

Targeted bulk RNA sequencing was performed using the HTG EdgeSeq Precision Immuno-Oncology Panel (HTG Molecular Diagnostics, Inc.). Briefly, tumour regions were macro dissected from paired pre-treatment biopsy and post-nivolumab resection

FFPE tissue sections and lysed using the HTG Sample Prep Kit according to the manufacturer's protocol. Following the EdgeSeq nuclease protection assay, libraries were generated, barcoded by PCR, pooled for Illumina sequencing, and processed using the HTG EdgeSeq Parser to generate gene-level expression counts for downstream analysis.

Targeted bulk RNA sequencing was performed for 18 of 19 patients with paired pre-NIVO and post-NIVO samples, excluding a single patient (20-002). A total of 42 samples (19 pre-treatment and 23 post-treatment samples) were initially profiled across a predefined panel of 1,410 immune-oncology-related genes. For patients with technical replicates, expression profiles were averaged prior to downstream analysis. Genes were filtered based on expression abundance, retaining genes with expression counts ≥5 in at least 20 samples, resulting in a final set of 1,396 genes. Following filtering and replicate consolidation, 18 matched pre-NIVO and 18 matched post-NIVO patient profiles were included for comparative analysis.

For each patient, treatment-associated transcriptional changes were quantified by calculating log2 fold-change in values between post-NIVO and pre-NIVO samples:

$$\log_2 FC = \log_2(\mathrm{Post}_{patient} + 1) - \log_2(\mathrm{Pre}_{patient} + 1)$$

Log2 fold-change matrices were standardized using z-score normalization prior to dimensionality reduction via principal component analysis (10PCs, Euclidean).

Clinical and pathological metadata were used to identify clinically annotated response anchor patients. Patients with ΔTIL = +1 were designated as response anchors, whereas patients with ΔTIL = −1 were designated as non-response anchors. These anchor groups were used as clinically annotated references for downstream analyses.

PC3 was selected for downstream response classification based on separation of clinically annotated anchor patients. Patients clustering with response anchor cases along PC3 were classified into the Response group, whereas patients clustering with non-response anchor cases were classified into the Non-response group. The resulting Response and Non-response patient classifications were used for all downstream comparative analyses.

Spatial transcriptomics data acquisition

A total of 189 tissue samples were obtained from 19 patients with head and neck squamous cell carcinoma (HNSCC) and profiled across two tumour microarrays (TMAs; TMA1 and TMA2). For each patient, TMA cores were sampled from multiple histological and treatment-defined regions, including pre-NIVO primary tumour, post-NIVO primary tumour, post-NIVO normal tissue (0.6mm diameter), and post-NIVO advancing tumour front (1.0mm diameter).

Tissue microarrays were constructed from respective standard of care formalin fixed paraffin embedded (FFPE) tissue blocks, using an automatic tissue arrayer (3DHISTECH TMA Grand Master), as previously described[32]. Briefly, haematoxylin and eosin–stained sections were assessed for identifiable areas of tumour in the donor block. Triplicate tumour cores (height= 4 mm; diameter= 1.0 mm and height = 4mm; diameter 0.6mm) were transferred from the donor block to the recipient block by a predetermined asymmetrical distribution. Haematoxylin and eosin–stained sections of the TMAs were examined to confirm accurate sampling and inclusion of representative tumour.

Formalin-fixed paraffin-embedded (FFPE) tissue sections were prepared for CosMx Spatial Molecular Imager (SMI; Bruker Spatial Biology) profiling according to the manufacturer's protocol. Briefly, FFPE blocks were sectioned at 5 µm, mounted onto Superfrost Plus Micro Slides (VWR), baked overnight at 37°C and stored at 4°C. Tissue sections were deparaffinized using xylene and ethanol clearance, followed by target retrieval in 1X Target Retrieval solution for 15 minutes at 100°C, and enzymatic digestion with Protease K at 40°C for 30 minutes. RNA targets were hybridized overnight at 37°C using the CosMx 6K Human Discovery Panel (Bruker Spatial Biology) before undergoing post-hybridization stringent washes. Following flow cell assembly and the addition of morphology markers (PanCK, CD45, CD3, B2M/CD298 antibodies) and DNA staining (DAPI), cyclic fluidics and multi-channel fluorescence imaging were performed on the CosMx (SMI) across selected fields of view (FOVs) using multi-slice Z-stacks. Subsequently, AtoMx Spatial Informatics Platform (SIP) was used to decode raw images into transcript coordinates. Cell boundaries were determined through the CosMx multi-modal segmentation pipeline driven by nuclear

and membrane staining. Following primary data processing, background noise filtering via negative control probes, and quality control filtering (excluding cells with <20 transcripts), a total of 391,229 single cells were profiled across all patients and regions prior to downstream transcript normalization. Most patients contributed 2–3 technical replicates per tissue region, enabling robust representation of spatial and treatment-associated variability. Because multiple tissue cores were profiled from most patients, analyses were performed at either the core or patient level, as appropriate for the specific analysis, with patient identity retained throughout the analysis workflow. This dataset was subsequently used for comparative analysis of cellular composition and spatial organization across treatment conditions and tissue compartments.

Preprocessing and batch correction

All downstream single-cell transcriptomic analyses were performed in Python (v3.12.8) using anndata (v0.12.6)[33] and scanpy (v1.11.5)[34], unless otherwise stated. Quality control metrics were computed using system control and negative control probe expression. Cells with greater than 5% expression of either control probe set were excluded from downstream analysis. Cells with fewer than 100 total counts and genes expressed in fewer than 400 cells were additionally removed. Fields of view (FOVs) containing fewer than 225 cells were excluded from further analysis.

Following preprocessing and quality filtering, 297,244 cells across 166 tissue cores were retained for downstream analyses. Expression counts were normalized to a total library size of 10,000 counts per cell and log-transformed using log1p normalization. Highly variable genes were identified using the Cell Ranger method, retaining the top 6,000 highly variable genes for downstream analysis.

Principal component analysis (PCA) was performed using 50 principal components. Batch correction and data integration across TMAs were performed using Harmony[35] with TMA identity specified as the batch variable. Uniform Manifold Approximation and Projection (UMAP)[36] was subsequently used for low-dimensional visualization of the integrated dataset.

Clustering and cell type annotation

A nearest-neighbour graph was constructed in the Harmony-corrected latent space using the Canberra distance metric to emphasize relative differences between feature values while reducing the influence of large-magnitude features during cell-to-cell similarity calculations. This was followed by Leiden clustering[37]. Multiple clustering resolutions were evaluated, and a Leiden resolution of 2 was selected for downstream analysis, resulting in 38 clusters.

Differential expression analysis was performed using the Wilcoxon rank-sum test to identify cluster-defining genes. Cell type annotations were assigned based on cluster-enriched differentially expressed genes and curated canonical marker gene sets. Clusters exhibiting strong tumour-associated signatures within post-NIVO normal regions were annotated as epithelial cells.

In addition to clusters identified as T cells through differential expression analysis, cells expressing any canonical T cell marker (*CD3D, CD3E, CD3G, or CD247*) with a log-normalized expression value above a threshold of 0.1 were additionally classified as T cells to ensure comprehensive identification of T cell populations. The threshold was selected to require expression above background while minimizing classification based on very low-level expression likely attributable to technical noise. This annotation strategy overall resulted in the identification of 13 major cell types for downstream analyses.

Removal of double negative T cells using machine learning

Following broad cell type annotation, 58,571 cells classified as T cells were isolated for focused downstream analysis. The same analytical workflow (PCA, Harmony integration across TMAs, Canberra distance-based neighbour graph construction, and UMAP embedding) was applied to the T cell subset analysis.

T cells were initially classified based on expression of canonical markers *CD4*, *CD8A*, and *CD8B*. Cells expressing *CD4* together with either *CD8A* or *CD8B* were annotated as $CD4^{+}CD8^{+}$ cells, whereas cells expressing only *CD4* or only *CD8A/CD8B* were annotated as $CD4^{+}CD8^{-}$ and $CD4^{-}CD8^{+}$ cells, respectively. Cells lacking detectable expression of both markers were annotated as $CD4^{-}CD8^{-}$ cells.

To resolve ambiguous $CD4^{-}CD8^{-}$ populations, a supervised Random Forest[38] classifier was trained using T cells with unambiguous $CD4^{+}CD8^{-}$ or $CD4^{-}CD8^{+}$ lineage assignment based on canonical marker expression (*CD4* for $CD4^{+}$ cells and *CD8A/CD8B* for $CD8^{+}$ cells) (**Supp Fig. 3A**). Expression values for *CD4*, *CD8A*, and *CD8B* were excluded from the feature set to avoid trivial classification. Input features included transcriptomic profiles, cellular morphology (area, aspect ratio, circularity, eccentricity, perimeter, nuclear morphology), sequencing quality metrics, spatial coordinates, and sample-level metadata (tumour type, patient identity, and TMA section).

The dataset was partitioned using a stratified 80:20 train–validation split. Quantitative features were standardized and categorical variables were ordinally encoded prior to model training. An initial Random Forest model (100 estimators) was used for feature ranking, and the top 200 features were retained for model refinement. A final Random Forest classifier (1,000 estimators, entropy criterion, class-weighted, max features = log2, minimum samples split = 20) was trained on the selected feature set.

Model performance was evaluated on the held-out validation set, achieving an area under the receiver operating characteristic curve (AUC) of 0.79. The trained classifier was then applied to $CD4^{-}CD8^{-}$ cells, with predicted labels assigned using a maximum class probability threshold of 0.52, which was empirically selected to balance classification confidence with retention of ambiguous $CD4^{-}CD8^{-}$ cells. Cells below this threshold retained their $CD4^{-}CD8^{-}$ label, while higher-confidence predictions were reassigned as $CD4^{+}CD8^{-}$ or $CD4^{-}CD8^{+}$ for downstream analyses.
Following classification, $CD4^{+}CD8^{-}$ and $CD4^{-}CD8^{+}$ T lineages showed improved separation in UMAP space compared to pre-resolved analyses, indicating a refined T lineage structure (**Supp Fig. 3B and 3C**). The resulting T lineage assignments were consistently distributed across patients, with both $CD4^{+}CD8^{-}$ (hereafter referred to as $CD4^{+}$ T cells) and $CD4^{-}CD8^{+}$ (hereafter referred to as $CD8^{+}$ T cells) populations detected across the cohort without patient-specific enrichment (**Supp Fig. 3D**), supporting stable lineage annotation for downstream analyses.

T cell sub-clustering and annotation

$CD4^+$ and $CD8^+$ T cell populations were independently isolated from the annotated T cell compartment for high-resolution subtype analysis. Each lineage-defined compartment was re-clustered independently using the same analytical framework, including PCA, Harmony integration across patients, neighbour graph construction using the Canberra distance metric, and UMAP embedding.

Multiple clustering resolutions were evaluated for each lineage, and a resolution of 1.5 was selected based on biological interpretability, providing clear separation of transcriptionally distinct cell populations while avoiding over-partitioning. This resulted in 16 $CD8^+$ and 17 $CD4^+$ T cell clusters. Differential expression analysis was performed using the Wilcoxon rank-sum test to identify cluster-specific marker genes. Based on canonical marker gene expression, clusters were annotated as various $CD8^+$ and $CD4^+$ T cell subtypes for downstream analyses.

Cell type composition and statistical analysis

Cluster-specific marker gene expression patterns were visualized using differential expression dot plots based on the top differentially expressed genes identified using the Wilcoxon rank-sum test.

Cell type and subtype distributions across patients and treatment conditions were summarized using proportional bar plots. Alluvial plots were generated to visualize changes in the relative abundance of each cell type between pre-NIVO and post-NIVO primary tumours within the Response and Non-response groups. Cell type proportions were normalized to the total number of cells within each response group and treatment condition.

For patient-level comparisons, the proportion of each cell type or subtype was calculated as the percentage of cells assigned to a particular cell type/subtype relative to the total number of cells within the corresponding sample. Samples were stratified into pre-NIVO Response (Pre-R), post-NIVO Response (Post-R), pre-NIVO Non-response (Pre-NR), and post-NIVO Non-response (Post-NR) groups. Paired comparisons between pre-NIVO and post-NIVO conditions within Response and Non-response cohorts were performed using paired Wilcoxon signed-rank tests. Boxplots

were used to visualize per-patient cell type proportions together with paired patient trajectories and associated p-values.

Patient-level subtype dynamics

$CD8^+$ T cell subtype dynamics across treatment were quantified at the patient level. For each patient and subtype, the proportion of cells belonging to a given subtype was calculated within each condition (Pre-NIVO and Post-NIVO) relative to the total $CD8^+$ T cell population in that sample.

Only patients with paired pre- and post-NIVO samples were included. Subtype dynamics were defined as the change in subtype proportion between post-NIVO and pre-NIVO conditions (Δ = Post − Pre). Patient level Δ values were visualized using heatmaps to summarize subtype-specific expansion or contraction across treatment and response groups.

Spatial positioning of $CD8^+$ T cells relative to tumour regions

Spatial proximity between $CD8^+$ T cells and tumour cells was quantified by calculating the Euclidean distance between the centroid pixel coordinates of each $CD8^+$ T cell and the centroid pixel coordinates of its nearest tumour cell. All spatial distances calculated in image pixel units (px) from CosMx spatial coordinates were converted to micrometres (μm) using the CosMx pixel resolution (1 px ≈ 0.120 μm). Cells in direct physical contact with tumour cells were defined as tumour-neighbouring cells (TN; B0) based on polygon-level adjacency derived from segmentation masks. Remaining $CD8^+$ T cells were stratified into discrete distance-based bins (B1–Bn) according to increasing distance from the nearest tumour.

To provide a complementary coarse grained representation of tumour proximity, $CD8^+$ T cells were additionally grouped into “Near” and “Far” compartments using a fixed distance threshold (<60 μm (500 px) and ≥ 60 μm (500 px), respectively).

$CD8^+$ T cell subtype composition within each spatial bin was computed as the fraction of cells belonging to a given subtype relative to the total $CD8^+$ T cell population in that bin, computed by pooling all $CD8^+$ T cells within each spatial bin. In contrast, for the

near–far compartment analysis, proportions were computed independently for each field of view (FOV) and subsequently summarised across samples per group for downstream comparisons. Statistical comparisons between conditions were performed using paired Wilcoxon signed-rank tests on FOV level proportions, and results were visualised using boxplots with per-sample values and associated p-values.

CD8⁺ spatial enrichment analysis

To characterize treatment associated spatial remodelling of CD8⁺ T cell states, CD8⁺ T cell subtype composition was quantified across tumour-distance bins separately for response and non-response groups. Distances were binned at 9 μm (75 px) intervals up to 240 μm (2,000 px) from the tumour.

For each distance bin and CD8⁺ T cell subtype, subtype proportions were calculated relative to the total number of CD8⁺ T cells within the same spatial bin and treatment condition. A spatial enrichment score was then defined as the difference in subtype proportion between post-treatment and pre-treatment conditions:

$$\text{Spatial enrichment score} = \mathrm{P}_{\mathrm{Post}} - \mathrm{P}_{\mathrm{Pre}}$$

where P represents the proportion of a given CD8⁺ T cell subtype relative to the total CD8⁺ T-cell population within a spatial distance bin.

Spatial enrichment scores were min-max scaled within each distance bin and visualized using stream plots to summarize subtype specific spatial enrichment or depletion patterns across tumour-distance gradients.

Spatial gene expression gradients

Spatial gene expression patterns were quantified across tumour–distance bins by aggregating cells based on their centroid-to-centroid distance from the nearest tumour cell. For each bin, mean expression of selected genes was computed to characterise transcriptional variation across spatial gradients relative to tumour proximity.

To enable comparison of spatial trends across genes, expression values were independently min–max scaled per gene across distance bins, allowing visualisation of relative spatial enrichment patterns independent of absolute expression magnitude.

Spatial gene expression dynamics were visualised using multiple complementary representations. Heatmaps were used to summarise gene expression gradients across distance bins. Mirrored lollipop plots were used to compare gene expression levels between response groups across tumour–distance compartments, highlighting differences in relative expression magnitude across spatial regions. Circular spatial shell plots were used to represent spatial gene expression structure across concentric tumour–distance compartments, where the innermost layer corresponds to tumour-proximal regions and successive outer shells represent increasing distance from the tumour boundary.

Spatial neighbourhood and niche analysis

To characterise the local microenvironment of $CD8^+$ T cells, spatial neighbourhoods were quantified using two complementary approaches: distance-based neighbourhoods and direct cell to cell contact neighbourhoods.

For distance based neighbourhoods, a spatial fingerprint was computed for each $CD8^+$ T cell based on the composition of surrounding cell types within a fixed radius neighbourhood (60 µm - 500 px – 7-8 cell diameters). For each query cell, the number of neighbouring cells of each annotated cell type within the defined radius was quantified, generating a cell-level neighbourhood feature vector representing local cellular composition. These spatial fingerprints were aggregated across all tissue sections to form a neighbourhood feature matrix. The matrix was normalised and used for dimensionality reduction via principal component analysis, followed by construction of a nearest-neighbour graph using Canberra distance. Leiden clustering was applied to identify recurrent spatial neighbourhood states. Spatial fingerprints were additionally used to compare the local cellular microenvironments surrounding selected $CD8^+$ T cell populations. For each comparison, the enrichment ratio for each neighbouring cell populations was calculated as the ratio of their mean abundances between groups.

Cluster-level neighbourhood profiles were summarised by averaging neighbour-type frequencies across cells within each cluster. Spatial niches were defined by assigning each cluster a label based on dominant neighbouring cell type composition. Clusters with strong enrichment for a single neighbouring population were annotated as cell type rich niches, whereas clusters with mixed neighbour contributions were classified as mixed niches.

In parallel, direct cell to cell interaction environments were characterised using contact-based neighbourhoods derived from segmentation defined polygon adjacency. For each $CD8^+$ T cell, directly contacting neighbouring cells were identified based on shared cell boundaries, and a contact fingerprint was constructed from the composition of these adjacent cell types. Contact niches were assigned based on the dominant contacting cell type per cell. Cells without detectable contacts were classified as “no contact” niches, while those with a dominant contacting population were annotated as cell type rich contact niches.

To quantify spatial niche dynamics associated with $CD8^+$ T cell remodelling across conditions, niche composition was summarised as the proportion of $CD8^+$ T cells assigned to each niche within predefined tumour-distance compartments (B0–B4). In addition, niche abundance was computed at the sample level by calculating the proportion of $CD8^+$ T cells occupying each niche within each tissue microarray core. Differences between response groups were assessed using Wilcoxon rank-sum tests on per sample niche proportions, and results were visualised using boxplots with sample-level values and statistical annotations.

Spatially constrained ligand–receptor interaction analysis

Ligand–receptor (LR) interactions were inferred between $CD8^+$ T cells, tumour cells, and fibroblasts within spatially defined tumour microenvironments. Analyses were restricted to these three major cellular compartments to focus on tumour–immune–stromal communication axes.

The tumour microenvironment was stratified into discrete spatial compartments based on $CD8^+$ T cell proximity to tumour cells, including a tumour-neighbour compartment

defined by direct physical contact (B0), and progressively increasing distance-based bins (B1–B4). Direct cellular contacts were defined using polygon-based adjacency derived from cell segmentation masks, such that neighbouring cells sharing a boundary were considered physically interacting (tumour-neighbour or contact-based interaction), whereas non-adjacent cells were assigned to distance-defined bins.

Within each spatial compartment, LR interactions were evaluated between all pairwise combinations of $CD8^+$ T cells, tumour cells, and fibroblasts. Interaction inference was performed using CellPhoneDB, incorporating permutation-based statistical testing and filtering based on ligand and receptor expression prevalence within the interacting populations.

To incorporate spatial information, LR interactions were retained only when ligand-expressing and receptor-expressing cells were located within the same spatial compartment or were directly adjacent based on polygon-level cell contacts, thereby restricting inferred interactions to spatially supported cellular neighbourhoods. Analyses were performed independently for the Response and Non-response groups within each spatial compartment.

For each ligand–receptor pair, interaction strength was quantified as the mean CellPhoneDB[39] interaction score within each group. A ΔLR score was defined as the difference in mean interaction strength between the Response groups and Non-response groups:

$$\Delta LR = LR_{NR} - LR_{R}$$

Ligand–receptor interactions were subsequently classified as Response-specific, Non-response-specific, or shared according to their statistical significance in each group (CellPhoneDB permutation test, $P < 0.05$). Interactions significant only in the Response group were classified as Response-specific, those significant only in the Non-response group as Non-response-specific, and those significant in both groups as shared. Results were visualised using bubble plots.

COMET 40-plex spatial proteomics analysis

Multiplexed spatial proteomics was performed using Lunaphore COMET 40-plex imaging across 106 tissue cores derived from 18 patients (excluding one patient, 2-041). Samples included matched pre-NIVO primary tumour, post-NIVO primary tumour, and post-NIVO normal tissue, encompassing a total of 147,424 single cells across all regions.

Raw protein expression matrices (40 markers including structural proteins and DAPI) were subjected to quality control and preprocessing. Cells with low total counts (<1000) were excluded. To account for variation in nuclear staining, DAPI-normalised protein expression was computed by dividing marker intensities by the corresponding DAPI signal per cell. The DAPI channel was subsequently removed from downstream analysis. The resulting expression matrix was further filtered to retain high-quality cells, yielding 145,170 cells for analysis.

Data were normalised using total-count normalisation followed by log-transformation. Principal component analysis followed by Harmony integration was performed using patient identity as the integration variable to reduce patient-specific technical variation while preserving shared biological structure across samples. A nearest-neighbour graph was constructed using the Canberra distance metric, followed by dimensionality reduction with UMAP.

Unsupervised clustering was performed using the Leiden algorithm (resolution = 0.5), and clusters were annotated into major cell types based on differentially expressed protein markers using Wilcoxon rank-sum tests.

To incorporate spatial context, $CD8^+$ T cell localisation relative to tumour regions was quantified using centroid-to-centroid Euclidean distance to the nearest tumour cell. Protein expression was analysed across tumour-distance gradients and visualised using marker expression profiles across distance bins.

External spatial transcriptomics validation set

A publicly available CosMx Spatial Molecular Imager (CosMx1k panel) dataset[40] of cutaneous squamous cell carcinoma treated with PD-L1 blockade was used for external validation. Patients received either cemiplimab (350 mg) or atezolizumab

(1200 mg), and samples comprised baseline, post-dose, and post-surgical tissue sections across 27 subjects represented on two TMAs. Pathological response annotations included 12 responders (mPR/pCR), 11 non-responders (non-mPR/pCR), and 4 subjects with unknown response status. The dataset contained 254,617 cells profiled across 1,000 genes. Notably, only 12 patients had matched baseline and post-dose samples, with early post-dose biopsy occurring after the first dose, comprising 6 responders (4 atezolizumab and 2 cemiplimab) and 6 non-responders (5 atezolizumab and 1 cemiplimab).

Data preprocessing, normalization, dimensionality reduction, batch correction, clustering, and cell-type annotation were performed using the same analytical framework applied to the primary CosMx6K cohort, including Harmony-based integration across TMAs, Canberra-distance nearest-neighbour graph construction, UMAP embedding, Leiden clustering, and differential expression-based cluster annotation. Following preprocessing, 205,461 cells were retained for downstream analyses.

T cell lineage annotation, double-negative T cell resolution, and $CD8^+$ T cell spatial analyses were performed as described for the primary cohort. Spatial proximity to tumour cells was quantified using centroid-to-centroid distance calculations, and spatial gene expression patterns were visualized across tumour-distance shells. Note all spatial distances calculated in image pixel units (px) from COMET spatial coordinates were converted to micrometres (μm) using the COMET pixel resolution (1 px ≈ 0.280 μm). As polygon-level segmentation boundaries were unavailable in this dataset, direct tumour-neighbour (B0) analyses could not be performed. Spatial niche analysis was therefore conducted using radius-based neighbourhood profiling (200-pixel radius), and niche composition patterns were compared across pathological response groups.

Explants: Tissue culture and Pembrolizumab treatment

Fresh human HNSCC tumour specimens were received immediately following surgical resection in tissue transfer buffer[24] and processed under sterile conditions. Tumour tissues were embedded in 4% low-melting-point agarose (Thermo Fisher Scientific, Cat. No. 16520050) and sectioned using a vibratome (Leica VT1200) to generate

precision-cut tumour slices of 300 µm thickness, according to predefined vibratome settings optimized for HNSCC specimens. Following sectioning, tumour slices were transferred into complete culture medium and allowed to recover for 2 hours. The slices were then embedded in hyaluronic acid-based hydrogels, as previously described by Adine et al.[24] and Fernando et al.[41], to support ex vivo preservation of tumour architecture and viability during culture. After the first day of ex-vivo culture, the culture medium was replaced with medium containing pembrolizumab at a final concentration of 5 µg/mL, which was kindly provided by NCCS. Tumour slices were maintained under treatment conditions for 5–7 days. At the end of treatment, slices were carefully retrieved from the hydrogels, fixed in 10% neutral buffered formalin, and subsequently processed for paraffin embedding to generate Formalin-fixed paraffin-embedded tissue sections for downstream histological and immunostaining analyses.

Explants: Immunofluorescence staining and image acquisition

Formalin-fixed paraffin-embedded tissue blocks were sectioned at 5 µm thickness using a microtome (Leica, HistoCore BIOCUT) and mounted onto glass slides for immunofluorescence staining. Paraffin tissue sections were dewaxed and subjected to heat-induced antigen retrieval in Tris-EDTA buffer, pH 9.0, using a microwave for 15 minutes at medium power, then allowed to cool at room temperature for 15 minutes. Sections were permeabilized in PBS-TX containing 0.1–0.5% Triton X-100 for 10 minutes, washed three times with PBS-TX, and blocked with 5% goat serum in PBS for 1 hour at room temperature.

Following blocking, sections were incubated overnight at 4°C with anti-human CD8a, together with the primary antibody for the marker of interest. All primary antibodies were diluted in PBS containing 0.1% goat serum. After primary antibody incubation, slides were washed three times with PBS for 5 minutes and incubated with the appropriate fluorophore-conjugated secondary antibodies. CD8 staining was detected using an Alexa Fluor™ 594 conjugated goat anti-mouse secondary antibody, while the marker of interest was detected using an Alexa Fluor™ 647/643 conjugated goat anti-rabbit secondary antibody. Following secondary antibody incubation, slides were washed three times with PBS for 5 minutes each in the dark. Pan-cytokeratin (PanCK) staining was performed sequentially after CD8 and marker of interest staining using directly conjugated Pan Cytokeratin monoclonal antibody, Alexa Fluor™ 488, diluted in PBS containing 0.1% goat serum, with overnight incubation at 4°C. Following

PanCK staining, slides were washed three times with PBS for 5 minutes each in the dark. Nuclei counterstaining was performed using DAPI diluted 1:4000 in PBS for 3 minutes, followed by three additional PBS washes. Coverslips were mounted onto the slides, and the slides were allowed to dry at room temperature for 30 minutes before storage at 4°C. Images were acquired using a Zeiss Axioscan 7 slide scanner with ZEN Blue software (v3.13).

Antibody	Conjugation	Source	Identifier	Concentration
CD8a monoclonal antibody	Unconjugated	Invitrogen	14-0085-82	1:100
Pan Cytokeratin	Alexa Fluor™ 488	Invitrogen	53-9003-82	1:200
LAG3	Unconjugated	Proteintech	80867-1-RR	1:100
CXCL8	Unconjugated	Proteintech	27095-1-AP	1:100
CXCL13	Unconjugated	Proteintech	86564-1-RR	1:100
KLF2	Unconjugated	Proteintech	23384-1-AP	1:100
PRF1	Unconjugated	Proteintech	14580-1AP	1:200
CCL5	Unconjugated	Proteintech	12000-1-AP	1:100

Explants: Image Analysis and Quantification

Whole-slide immunofluorescence images were exported from ZEN Blue software and analysed using QuPath (v0.7.0), where nuclei segmentation was performed using the DAPI channel and cells were detected using the watershed algorithm. The resulting single-cell immunofluorescence data were exported and further processed using custom Python scripts. To remove imaging artefacts and low-quality detections, cells with extreme total fluorescence intensities (5th–99th percentile) or nuclear staining intensities (<5th percentile or >99.5th percentile) were excluded. To account for technical variation in staining and image acquisition across tissue sections, marker intensities were normalized to the median DAPI intensity on a per-cell basis. Following normalization, the DAPI channel was removed from downstream analyses and marker intensities were log-transformed.

Tumour and $CD8^+$ T cell populations were identified using marker expression thresholds derived from the processed immunofluorescence signals. Tumour cells were defined by Pan-cytokeratin (PanCK) expression, with positivity determined using an adaptive threshold based on the mean and standard deviation of clipped PanCK

intensities. $CD8^+$ T cells were identified using percentile-based gating of CD8 signal intensity while excluding PanCK-positive tumour cells.

For spatial analyses, the Euclidean distance from each $CD8^+$ T cell to the nearest tumour cell was calculated. Distances were normalized to the maximum tumour distance observed within each specimen to enable comparisons across explants of different sizes and grouped into equal relative distance bins. The mean expression of the marker of interest within $CD8^+$ T cells was subsequently min–max normalized across distance bins to facilitate comparison of spatial expression gradients between samples. Spatial trends were visualized using the circular spatial shell plots described above.

Data Availability

The raw and processed CosMx6k spatial transcriptomic, targeted bulk RNA sequencing, whole-genome sequencing, and COMET spatial proteomic datasets generated and analyzed during this study have been deposited in the appropriate public repositories under the following accession numbers: CosMx spatial transcriptomics, [GSE341950]; bulk RNA sequencing, [repository and accession]; whole-genome sequencing, [repository and accession]; and COMET spatial proteomics, [repository and accession]. The datasets will be publicly available upon publication. Clinical metadata have been de-identified to protect participant privacy.

Code Availability

All code used for data preprocessing, quality control, cell type annotation, spatial analyses, differential expression analyses, ligand–receptor interaction analyses, machine learning, statistical analyses, and figure generation is publicly available through GitHub at [https://github.com/LakshmiAlagappan/HNSCC_NICO_Spatial]. A permanent archived version of the repository corresponding to the version used in this study is available through Zenodo (DOI: 10.5281/zenodo.21700647). All software packages, algorithms, and their versions used in this study are described in the Methods.

Acknowledgements

We would like to thank all patients, donors and families who contributed to this project. This project was funded through the following grants awarded to NGI [National Medical Research Council (Singapore) Clinician Scientist Individual Research Grant (MOH-001701-00) Singapore Translational Researcher award (MOH-001684-00), and the Peter Fu Head and Neck Cancer Program (National Cancer Centre Singapore)], to JS [Bristol Myer Squibb (BMS) Investigator-led trial funding (CA209-891)], and to AS [Innovate UK funding for NICO WGS in association with Genomics England].

The authors wish to acknowledge the considerable contribution of the following centres and individuals in the design, conduct and delivery of the NICO clinical trial; Liverpool Clinical Trials Centre (LCTC), Clatterbridge Cancer Centre (CCC) for sponsorship of the NICO trial, the recruiting clinicians of the Liverpool Head & Neck Centre (LHNC), Aintree University Hospital, Clatterbridge Cancer Centre (CCC), the Beatson West of Scotland Cancer Centre and Queen Elizabeth University Hospital Glasgow, Bristol Myer Squibb (BMS), trial funder, Innovate UK, grant award for NICO Genomics England WGS processing, and the Liverpool University Biobank (LUB) & GCP Laboratory for bioresource and clinical trial sample-curation, processing and storage.

No AI tools were used for data analysis, figure generation, or drawing of specific conclusions. All AI-generated text was reviewed and edited by the authors, who take full responsibility for the content.

Authors Contributions

LA, RB, CC, JS, AS and NGI conceptualized and designed the study, and interpreted the data. LA, LA, HSQ, FK, JY, NZW, CJ, LYC performed the experiments, and supervised by ELSF, PJY and NGI. RB, JS, AS, AH, CP, JMcC, MF, CR, RJ, JG, JP and MM were involved in the conduct of the trial, MR and KH provided pathologic analyses and curation of case samples prior to construction of the TMA. CO provided translational workflow design and analysis. FGD undertook tissue and TMA preparation, and performed experiments. JT and IR provided bioinformatic support for bulk RNAseq and WGS workflows. TP undertook laboratory-based analyses. LA

carried out bioinformatic analyses under supervision by CC. LA drafted the manuscript; LA, AS and NGI critically revised and approved the final version.

Competing Interests

NGI sits on the Scientific Advisory Boards of VerImmune and Vivo Surgical and has received honoraria/funding from Merck/MSD and Innokeys, all of which are outside the scope of this submitted work. AS has sat on Scientific Advisory Boards and Consultancy Panels for MSD, receiving associated honoraria. JJS has received honoraria (personal and institution) for participation in advisory boards from BMS, Immunocore, Replimune, Pierre Fabre and Delcath, has received support for travel/conference attendance from BMS, MSD and Replimune, and has received grant income (to institution) for clinical trials from BMS, AZ and Immunocore. MDF reports research grants from AstraZeneca (Inst), Boehringer Ingelheim (Inst) and MSD (Inst); non-exec board member for Curacell; holds appointments with DRA and HCA; and has received honoraria for advisory and consultancy work from Accord, Amgen, AstraZeneca, BeOne, Boxer, Celgene, GSK, Guardant Health, Immutep, Janssen, Merck, MSD, Oxford VacMedix, Regeneron, Roche, Societe Generale, Syncorp and Transgene; he is supported by the UCL/UCLH NIHR Biomedical Research Centre. FG is an employee of Miltenyi Biotec. The remaining authors declare no other competing interests.

References

1. Topalian, S. L. *et al.* Safety, Activity, and Immune Correlates of Anti–PD-1 Antibody in Cancer. *New England Journal of Medicine* **366**, 2443–2454 (2012).
2. Forde, P. M. *et al.* Neoadjuvant PD-1 Blockade in Resectable Lung Cancer. *New England Journal of Medicine* **378**, 1976–1986 (2018).
3. Ribas, A. & Wolchok, J. D. Cancer immunotherapy using checkpoint blockade. *Science* **359**, 1350–1355 (2018).
4. Patel, S. P. *et al.* Neoadjuvant–Adjuvant or Adjuvant-Only Pembrolizumab in Advanced Melanoma. *New England Journal of Medicine* **388**, 813–823 (2023).

5. Sung, H. *et al.* Global Cancer Statistics 2020: GLOBOCAN Estimates of Incidence and Mortality Worldwide for 36 Cancers in 185 Countries. *CA Cancer J Clin* **71**, 209–249 (2021).
6. Cohen, E. E. W. *et al.* Pembrolizumab versus methotrexate, docetaxel, or cetuximab for recurrent or metastatic head-and-neck squamous cell carcinoma (KEYNOTE-040): a randomised, open-label, phase 3 study. *Lancet* **393**, 156–167 (2019).
7. Burtness, B. *et al.* Pembrolizumab alone or with chemotherapy versus cetuximab with chemotherapy for recurrent or metastatic squamous cell carcinoma of the head and neck (KEYNOTE-048): a randomised, open-label, phase 3 study. *Lancet* **394**, 1915–1928 (2019).
8. Uppaluri, R. *et al.* Neoadjuvant and Adjuvant Pembrolizumab in Resectable Locally Advanced, Human Papillomavirus-Unrelated Head and Neck Cancer: A Multicenter, Phase II Trial. *Clin Cancer Res* **26**, 5140–5152 (2020).
9. Wise-Draper, T. M. *et al.* Phase II Clinical Trial of Neoadjuvant and Adjuvant Pembrolizumab in Resectable Local-Regionally Advanced Head and Neck Squamous Cell Carcinoma. *Clin Cancer Res* **28**, 1345–1352 (2022).
10. Uppaluri, R. *et al.* Neoadjuvant and Adjuvant Pembrolizumab in Locally Advanced Head and Neck Cancer. *New England Journal of Medicine* **393**, 37–50 (2025).
11. Cohen, E. E. W. *et al.* The Society for Immunotherapy of Cancer consensus statement on immunotherapy for the treatment of squamous cell carcinoma of the head and neck (HNSCC). *J Immunother Cancer* **7**, 184 (2019).
12. Topalian, S. L., Taube, J. M. & Pardoll, D. M. Neoadjuvant checkpoint blockade for cancer immunotherapy. *Science* **367**, eaax0182 (2020).
13. Oliveira, G. *et al.* Preexisting tumour-resident T cells with cytotoxic potential associate with response to neoadjuvant anti-PD-1 in head and neck cancer. *Sci Immunol* **8**, eadf4968 (2023).
14. Wei, S. C. *et al.* Distinct Cellular Mechanisms Underlie Anti-CTLA-4 and Anti-PD-1 Checkpoint Blockade. *Cell* **170**, 1120-1133.e17 (2017).
15. Ståhl, P. L. *et al.* Visualization and analysis of gene expression in tissue sections by spatial transcriptomics. *Science* **353**, 78–82 (2016).
16. Moncada, R. *et al.* Integrating microarray-based spatial transcriptomics and single-cell RNA-seq reveals tissue architecture in pancreatic ductal adenocarcinomas. *Nat Biotechnol* **38**, 333–342 (2020).

17. Liu, J. *et al.* Improved Efficacy of Neoadjuvant Compared to Adjuvant Immunotherapy to Eradicate Metastatic Disease. *Cancer Discov* **6**, 1382–1399 (2016).
18. Liu, J. *et al.* Timing of neoadjuvant immunotherapy in relation to surgery is crucial for outcome. *Oncoimmunology* **8**, e1581530 (2019).
19. Liu, J. *et al.* Batf3+ DCs and type I IFN are critical for the efficacy of neoadjuvant cancer immunotherapy. *Oncoimmunology* **8**, e1546068 (2019).
20. Blank, C. U. *et al.* Neoadjuvant versus adjuvant ipilimumab plus nivolumab in macroscopic stage III melanoma. *Nat Med* **24**, 1655–1661 (2018).
21. Schoenfeld, J. D. *et al.* Neoadjuvant Nivolumab or Nivolumab Plus Ipilimumab in Untreated Oral Cavity Squamous Cell Carcinoma: A Phase 2 Open-Label Randomized Clinical Trial. *JAMA Oncol* **6**, 1563–1570 (2020).
22. Brooker, R. C., Schache, A. G. & Sacco, J. J. NICO Phase II clinical trial - focus on an emerging immunotherapy strategy for the adjuvant treatment of locally-advanced oral cancers. *Br J Oral Maxillofac Surg* **59**, 959–962 (2021).
23. McInnes, L., Healy, J., Saul, N. & Großberger, L. UMAP: Uniform Manifold Approximation and Projection. *Journal of Open Source Software* **3**, 861 (2018).
24. Adine, C. *et al.* Bioengineered hydrogels enhance *ex vivo* preservation of patient-derived tumour explants for drug evaluation. *Biomaterials* **305**, 122460 (2024).
25. Siddiqui, I. *et al.* Intratumoural Tcf1+PD-1+CD8+ T Cells with Stem-like Properties Promote Tumour Control in Response to Vaccination and Checkpoint Blockade Immunotherapy. *Immunity* **50**, 195-211.e10 (2019).
26. Yost, K. E. *et al.* Clonal replacement of tumour-specific T cells following PD-1 blockade. *Nat Med* **25**, 1251–1259 (2019).
27. Cabrita, R. *et al.* Tertiary lymphoid structures improve immunotherapy and survival in melanoma. *Nature* **577**, 561–565 (2020).
28. Helmink, B. A. *et al.* B cells and tertiary lymphoid structures promote immunotherapy response. *Nature* **577**, 549–555 (2020).
29. Fridman, W. H. *et al.* B cells and tertiary lymphoid structures as determinants of tumour immune contexture and clinical outcome. *Nat Rev Clin Oncol* **19**, 441–457 (2022).

30. Mariathasan, S. *et al.* TGFβ attenuates tumour response to PD-L1 blockade by contributing to exclusion of T cells. *Nature* **554**, 544–548 (2018).
31. Binnewies, M. *et al.* Understanding the tumour immune microenvironment (TIME) for effective therapy. *Nat Med* **24**, 541–550 (2018).
32. Parsons, M. & Grabsch, H. How to make tissue microarrays. *Diagnostic Histopathology* **15**, 142–150 (2009).
33. Virshup, I., Rybakov, S., Theis, F. J., Angerer, P. & Wolf, F. A. anndata: Access and store annotated data matrices. *Journal of Open Source Software* **9**, 4371 (2024).
34. Wolf, F. A., Angerer, P. & Theis, F. J. SCANPY: large-scale single-cell gene expression data analysis. *Genome Biol* **19**, 15 (2018).
35. Korsunsky, I. *et al.* Fast, sensitive and accurate integration of single-cell data with Harmony. *Nat Methods* **16**, 1289–1296 (2019).
36. McInnes, L., Healy, J., Saul, N. & Großberger, L. UMAP: Uniform Manifold Approximation and Projection. *Journal of Open Source Software* **3**, 861 (2018).
37. Traag, V. A., Waltman, L. & van Eck, N. J. From Louvain to Leiden: guaranteeing well-connected communities. *Sci Rep* **9**, 5233 (2019).
38. Breiman, L. Random Forests. *Machine Learning* **45**, 5–32 (2001).
39. Efremova, M., Vento-Tormo, M., Teichmann, S. A. & Vento-Tormo, R. CellPhoneDB: inferring cell-cell communication from combined expression of multi-subunit ligand-receptor complexes. *Nat Protoc* **15**, 1484–1506 (2020).
40. Lee, M. Y. *et al.* Single-cell spatial transcriptomics uncovers niches that govern response to PD-1/PD-L1 blockade in cutaneous squamous cell carcinoma. *J Immunother Cancer* **14**, e014067 (2026).
41. Fernando, K. *et al.* Extended human lymph node explants for evaluation of adaptive immunity. *Trends in Biotechnology* **43**, 3134–3153 (2025).

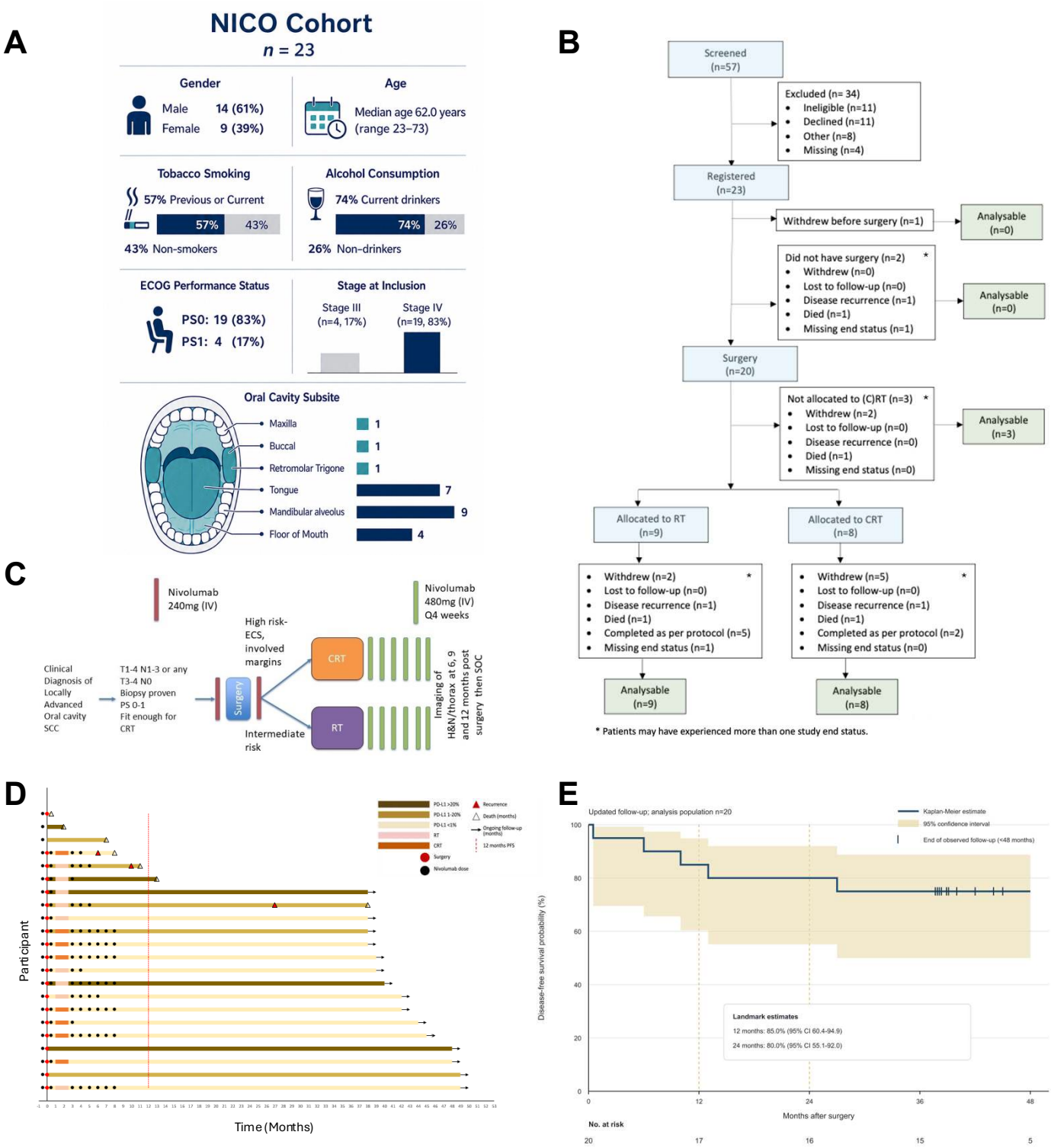

Figure 1 - NICO clinical trial parameters and associated trial-related outcomes
A – NICO Cohort Description (clinical & demographic features)
B – CONSORT diagram of NICO participants from screening to completion of adjuvant trial regime.
C – Schematic diagram of NICO trial treatment schedule†.
D – Swimmers Plot detailing the clinical course for each participant from point of neoadjuvant dosing. Individual per protocol treatments are each identified. Colour coding is based on the primary tumour PDL1 staining classification (Central blinded independent reporting; Dako PD-L1 IHC 28-8 pharmDx assay).
Clinical events are depicted in line with treatment time course.
E – Kaplan-Meier estimate plot of Disease Free Survival (DFS; death from any cause or first recurrence) measured in months from the time of surgery. The primary endpoint for the NICO phase II trial was DFS at 12 months, reanalysis of NICO cohort provides updated DFS probabilities at 12 & 24 months as indicated by red dotted lines.

†modified from Brooker RC, Schache AG, Sacco JJ. NICO Phase II clinical trial - focus on an emerging immunotherapy strategy for the adjuvant treatment of locally-advanced oral cancers.
Br J Oral Maxillofac Surg. 2021 Oct;59(8):959-962. doi: 10.1016/j.bjoms.2020.08.059

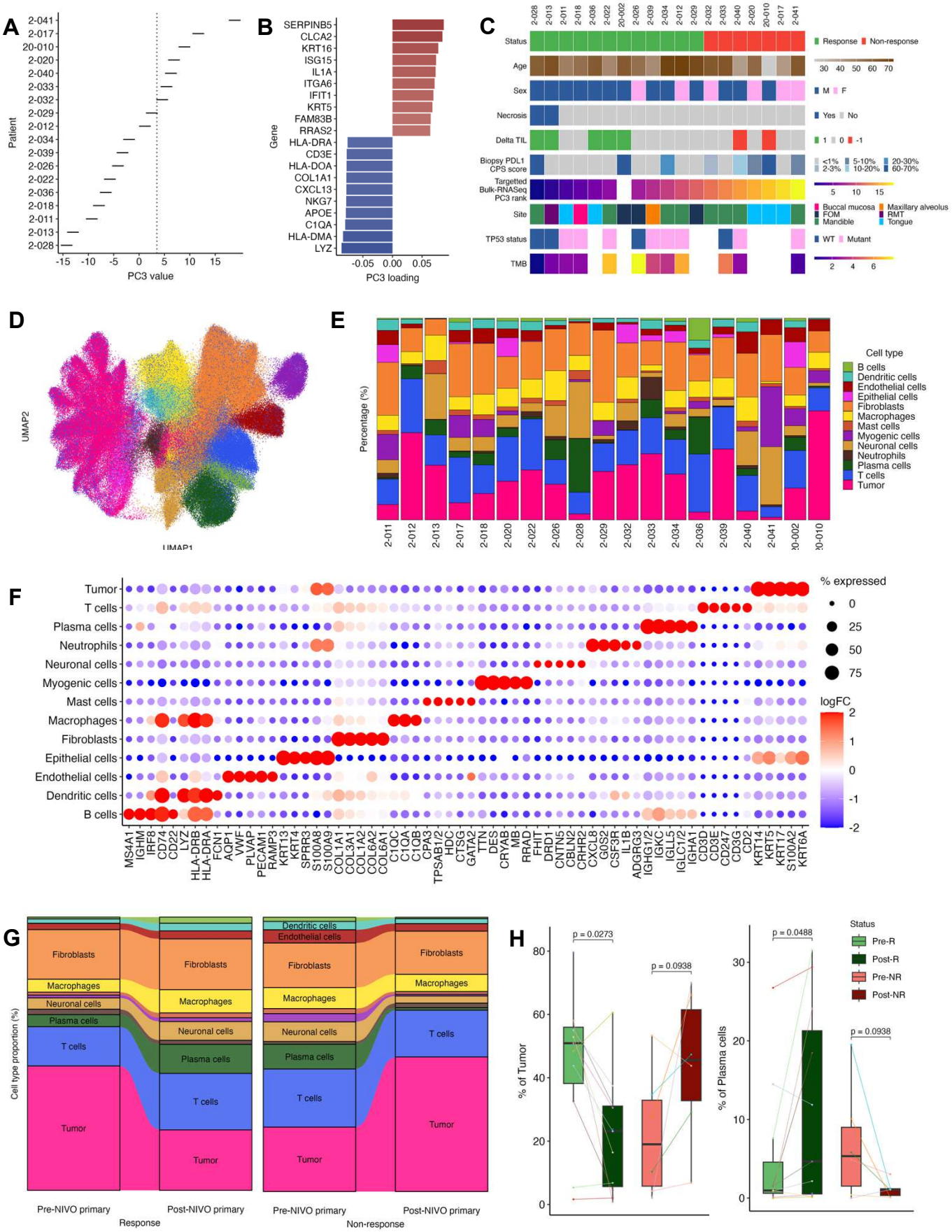

Figure 2. Targeted Bulk RNA-seq–guided response stratification and single-cell spatial transcriptomic atlas of the tumour microenvironment.

(A) Patient ranking based on PC3 scores derived from bulk RNA-seq principal component analysis. The dashed line indicates the threshold used to classify patients into the Response and Non-response groups.

(B) Genes with the strongest positive and negative loadings on PC3, highlighting the principal transcriptional features underlying patient classification

(C) Patient-level summary of clinical, molecular and pathological characteristics, ordered by PC3 score and response status

(D) UMAP representation of the CosMx 6K single-cell spatial transcriptomic dataset, coloured by cell type.

(E) Stacked bar plot showing the relative cell type composition across patients

(F) Dot plot of canonical marker genes used for major cell type annotation.

(G) Alluvial plots illustrating treatment-associated changes in cell type proportions between pre-NIVO and post-NIVO primary tumour samples, pooled across patients within the Response and Non-response groups..

(H) Box plots showing the proportions of major cell types in pre-NIVO Response (Pre-R), post-NIVO Response (Post-R), pre-NIVO Non-response (Pre-NR) and post-NIVO Non-response (Post-NR) primary tumour samples. Individual patients are connected by lines between matched pre- and post-NIVO samples within each response group, and statistical comparisons were performed using paired Wilcoxon signed-rank tests.

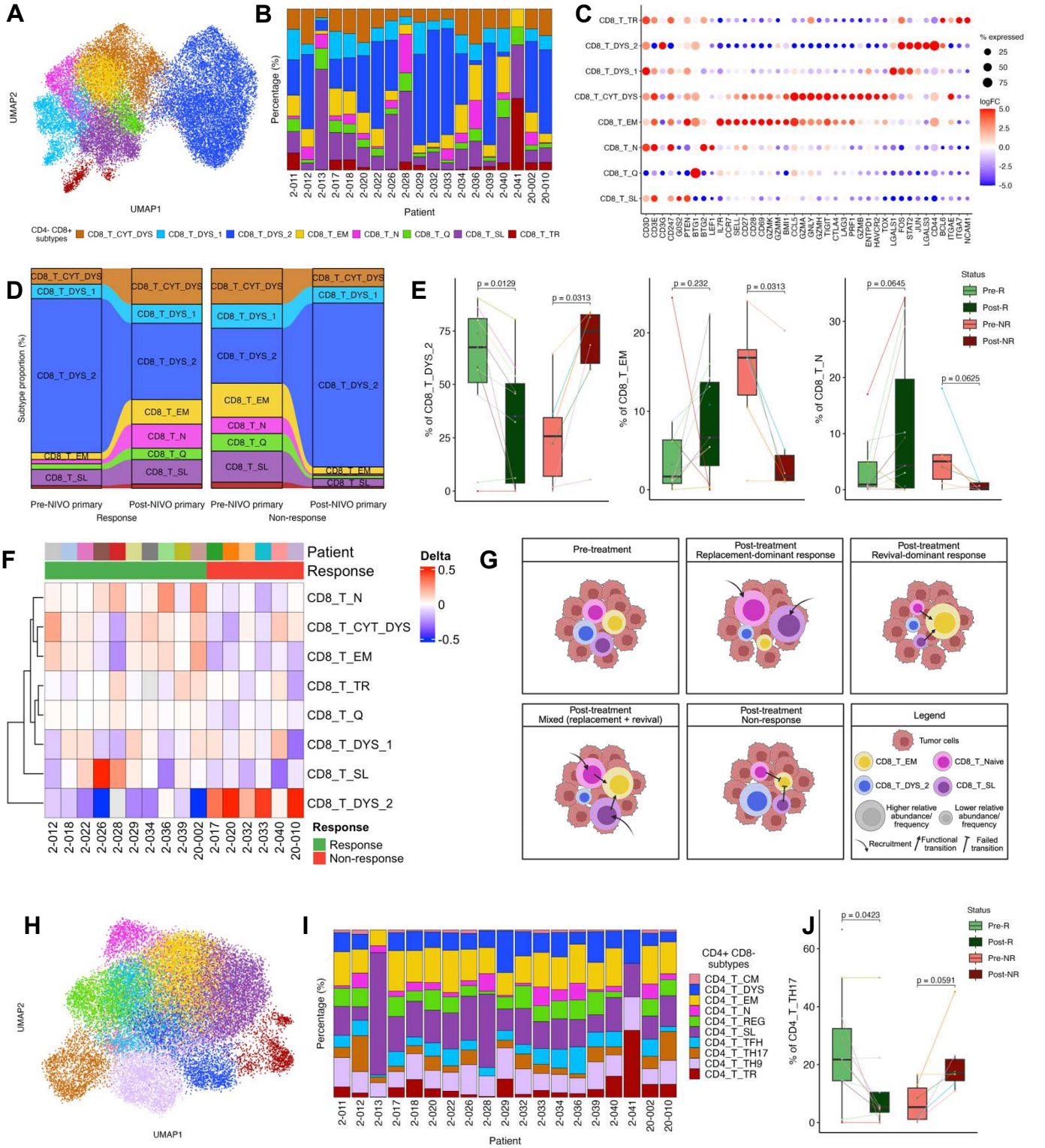

Figure 3. T cell lineage resolution reveals distinct CD8⁺ and CD4⁺ T cell remodelling programs associated with treatment response.
(A) UMAP representation of CD8⁺ T cells coloured by annotated subtype.
(B) Stacked bar plot showing the percentage of each CD8⁺ T cell subtype in individual patients.
(C) Dot plot of canonical marker genes used for CD8⁺ T cell subtype annotation.
(D) Alluvial plots illustrating treatment-associated changes in CD8⁺ T cell subtype proportions between pre-NIVO and post-NIVO primary tumour samples, pooled across patients within the Response and Non-response groups.
(E) Box plots showing the proportions of CD8⁺ T cell subtypes across pre-NIVO Response (Pre-R), post-NIVO Response (Post-R), pre-NIVO Non-response (Pre-NR) and post-NIVO Non-response (Post-NR) primary tumour samples. Individual patients are connected by lines between matched pre- and post-NIVO samples within each response group. Statistical comparisons were performed using paired Wilcoxon signed-rank tests.
(F) Heatmap showing paired changes (ΔPost–Pre) in CD8⁺ T cell subtype proportions across individual patients, summarizing treatment-associated remodelling within the Response and Non-response groups. CD8⁺ T cell subtypes are hierarchically clustered, and patients are ordered by response status.
(G) Schematic summary of recurrent response-associated CD8⁺ T cell remodelling archetypes, including replacement-dominant, revival-like and mixed patterns.
(H) UMAP representation of CD4⁺ T cells coloured by annotated subtype.
(I) Stacked bar plot showing the percentage of each CD4⁺ T cell subtype in individual patients.
(J) Box plots showing the proportions of CD4_T_Th17 cells across pre-NIVO Response (Pre-R), post-NIVO Response (Post-R), pre-NIVO Non-response (Pre-NR) and post-NIVO Non-response (post-NR) primary tumour samples. Individual patients are connected by lines between matched pre- and post-NIVO samples within each response group. Statistical comparisons were performed using paired Wilcoxon signed-rank tests.

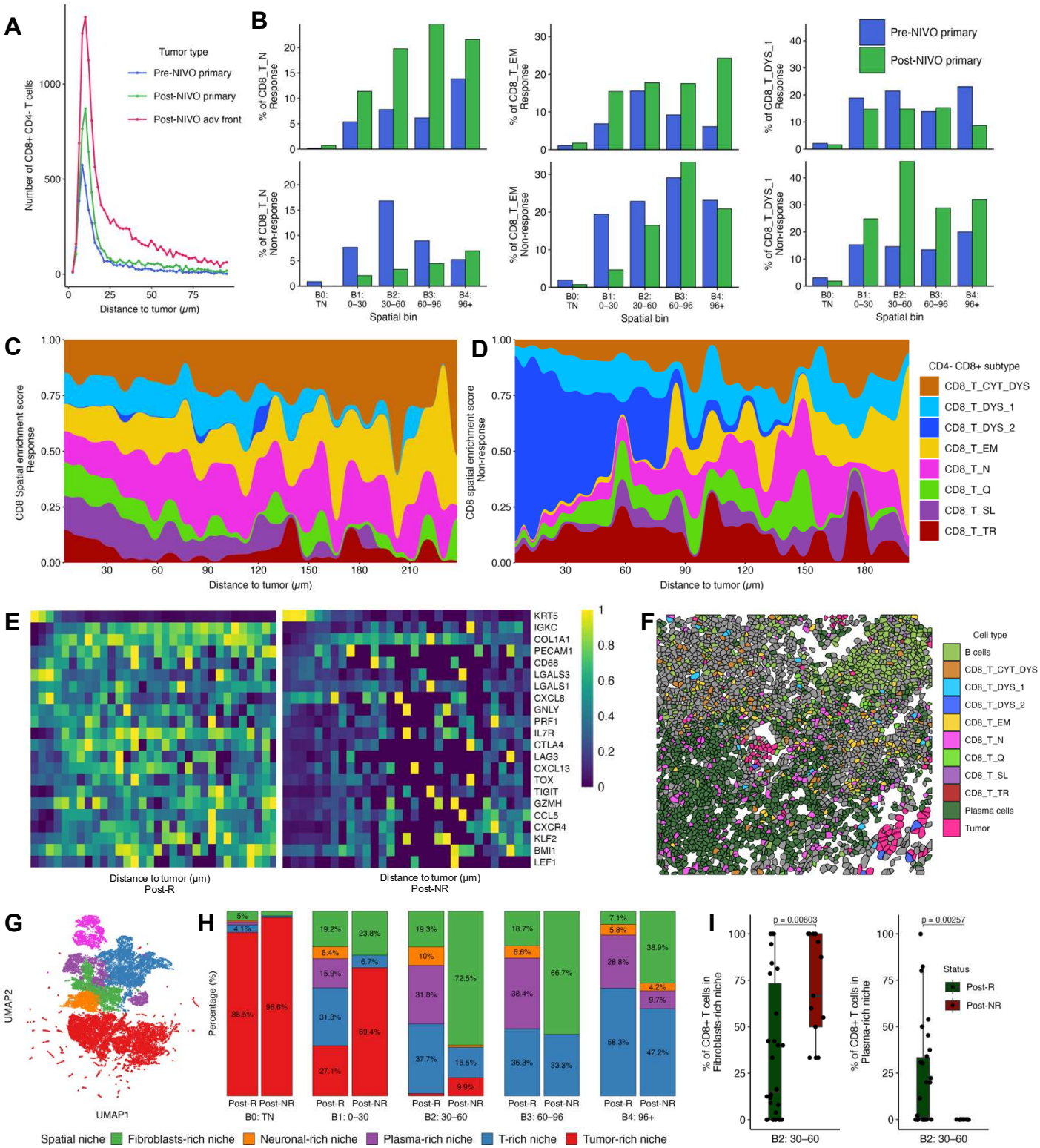

Figure 4. Spatial organization, transcriptional programs, microenvironmental niches and ligand–receptor interactions define response-associated CD8⁺ T cell states.
(A) Line plot showing the distribution of CD8⁺ T cells as a function of distance to tumour (μm) across pre-NIVO primary, post-NIVO primary and post-NIVO advancing front tumour samples.
(B) Bar plots showing the proportions of selected CD8⁺ T cell subtypes (CD8_T_N, CD8_T_EM and CD8_T_DYS_1) across distance to tumour spatial bins (B0–B4) in pre-NIVO and post-NIVO primary tumour samples from the Response and Non-response groups.
(C–D) Stream plots showing treatment-associated spatial enrichment of CD8⁺ T cell subtypes across distance to tumour in the Response (C) and Non-response (D) groups. Spatial enrichment scores were calculated as the change in subtype proportion between post-NIVO and pre-NIVO samples within each distance to tumour bin and are shown after min–max normalization.
(E) Heatmap showing spatial gene expression gradients across distance to tumour in post-NIVO primary tumour samples from the Response (Post-R) and Non-response groups (Post-NR). Gene expression was min–max normalized across distance bins for each gene.
(F) Representative spatial reconstruction from a Response sample showing the spatial distribution of CD8⁺ T cell subtypes relative to tumour cells, plasma cells and B cells.
(G) UMAP representation of CD8⁺ T cells associated distance-based neighbourhood coloured by spatial niche annotation derived from local cellular composition.
(H) Stacked bar plots showing the proportions of distance-based CD8⁺ T cell spatial niches across distance to tumour bins in post-NIVO Response and post-NIVO Non-response primary tumour samples
(I) Box plots showing the percentage of CD8⁺ T cells localized within fibroblast-rich and plasma cell-rich niches in the B2 (30–60 μm) distance to tumour compartment of post-NIVO primary tumour samples. Each dot represents one tissue core. Statistical comparisons were performed using Wilcoxon rank-sum tests.

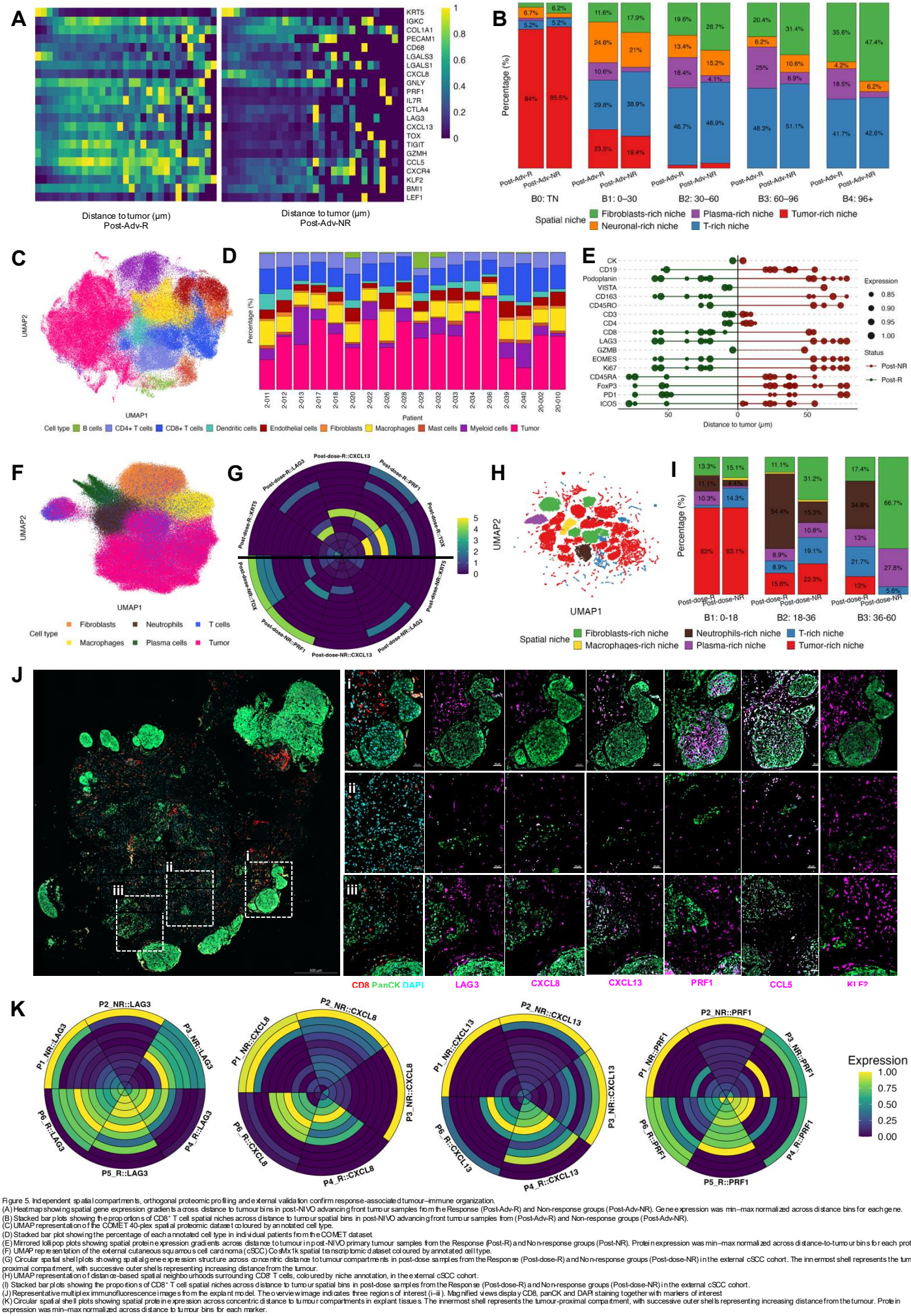

Figure 5. Independent spatial compartments, orthogonal proteomic profiling and external validation confirm response-associated tumour–immune organization.
(A) Heatmap showing spatial gene expression gradients across distance to tumour bins in post-NIVO advancing front tumour samples from the Response (Post-Adv-R) and Non-response groups (Post-Adv-NR). Gene expression was min–max normalized across distance bins for each gene.
(B) Stacked bar plots showing the proportions of CD8⁺ T cell spatial niches across distance to tumour spatial bins in post-NIVO advancing front tumour samples from (Post-Adv-R) and Non-response groups (Post-Adv-NR).
(C) UMAP representation of the COMET 40-plex spatial proteomic dataset coloured by annotated cell type.
(D) Stacked bar plot showing the percentage of each annotated cell type in individual patients from the COMET dataset.
(E) Mirrored lollipop plots showing spatial protein expression gradients across distance to tumour in post-NIVO primary tumour samples from the Response (Post-R) and Non-response groups (Post-NR). Protein expression was min–max normalized across distance-to-tumour bins for each protein.
(F) UMAP representation of the external cutaneous squamous cell carcinoma (cSCC) CosMx 1k spatial transcriptomic dataset coloured by annotated cell type.
(G) Circular spatial shell plots showing spatial gene expression structure across concentric distance to tumour compartments in post-dose samples from the Response (Post-dose-R) and Non-response groups (Post-dose-NR) in the external cSCC cohort. The innermost shell represents the tumour-proximal compartment, with successive outer shells representing increasing distance from the tumour.
(H) UMAP representation of distance-based spatial neighborhoods surrounding CD8⁺ T cells, coloured by niche annotation, in the external cSCC cohort.
(I) Stacked bar plots showing the proportions of CD8⁺ T cell spatial niches across distance to tumour spatial bins in post-dose samples from the Response (Post-dose-R) and Non-response groups (Post-dose-NR) in the external cSCC cohort.
(J) Representative multiplex immunofluorescence images from the explant model. The overview image indicates three regions of interest (i–iii). Magnified views display CD8, panCK and DAPI staining together with markers of interest.
(K) Circular spatial shell plots showing spatial protein expression across concentric distance to tumour compartments in explant tissues. The innermost shell represents the tumour-proximal compartment, with successive outer shells representing increasing distance from the tumour. Protein expression was min–max normalized across distance to tumour bins for each marker.

Supplementary Files

This is a list of supplementary files associated with this preprint. Click to download.

- Supplementary.docx
- NICOFinalStatisticalAnalysisReportAddendumV1.020230228.pdf
- SSNICPROTOCOL.5NICOProtocol.pdf
- Supplementaryfigures.pdf
- NICOFinalStatisticalAnalysisReportV1.020241028.pdf